



On the influence of time-dependent behaviour of elastomeric wave energy harvesting membranes using experimental and numerical modelling techniques

Ieuan Collins^a, Marco Contino^b, Claudia Marano^b, Ian Masters^a, Mokarram Hossain^{a,*}

^a Zienkiewicz Centre for Computational Engineering (ZCCE), Faculty of Science and Engineering, Swansea University, SA1 8EN, United Kingdom

^b Polymer Engineering Laboratory, Department of Chemistry, Materials and Chemical Engineering, Politecnico di Milano, 20133 Milano, Italy

ARTICLE INFO

Keywords:

Natural rubbers
Material characterisation
Non-linear evolution equation
Finite strain viscoelasticity
Finite element modelling
Flexible wave energy converter (FlexWEC)

ABSTRACT

The transient response of elastomeric polymers is dependent on polymer composition, temperature and the loading history. In particular, hysteresis, dissipation and creep are significant in the choice of material for elastomer membrane wave energy converters. Natural rubber is a good candidate when looking for material for a wave energy harvester since it has an excellent stretchability, is almost resistant to the environment in which the harvester will be used and has good fatigue properties. The mechanical behaviour of the natural rubber used in this work has been deeply characterised: the material resulted to have a very little hysteretical behaviour (that is a very low energy dissipation during stretching) but also to show a strain-dependency, stress softening, and relaxation at constant stretch. Low dissipation represents the best case scenario for energy harvesting; in reality reinforcement of the material is required which adds to the dissipative behaviour. Afterwards, an extended finite strain viscoelastic constitutive model is proposed that is calibrated analytically to the experimental data to identify the relevant material parameters resulting in non-linear viscosity functions in the evolution equations of the constitutive model. The model was able to capture the minimal dissipation behaviour with good degrees of accuracy. Results are shown for a flexible membrane wave energy converter under creep and cyclic loading. A parametric study is made comparing the experimentally characterised polymer with different amounts of viscous dissipation. The response of the wave energy converter shows that even minimal amounts of dissipation manifests itself into changes in the pressure–volume function and reduction in energy capture through hysteresis. The new material model shows, for the first time, that the control of internal pressure in wave energy membranes must take into account transient material effects.

1. Introduction

Natural rubbers, along with other elastomeric materials, are great candidates for the emerging trend of flexible energy harvesting polymers. Over the past decade, there has been a focus on optimising energy harvesting devices by making use of structural flexibility. Large membranes, for instance, can be employed in ocean energy harvesting devices; see Collins et al. (2021, 2019) and Moretti et al. (2020) for extensive reviews of flexible membrane-based energy harvesters. Wind and tidal systems are able to utilise flexible blades comprised of deformable and rigid polymers, see Hoerner et al. (2021a,b) and Fu et al. (2020). The primary reason for utilising flexible structures is to increase the efficiency of energy harvesting while reducing structural loads to improve the fatigue life and reduce the cost of the device. Natural rubbers are the ideal candidate materials due to their unique qualities

of high levels of stretchability, usable over a wide range of temperatures, resistant to various degradation phenomena, and characterised by a great fatigue resistance. Despite these excellent properties, their mechanical behaviour is very nonlinear (physically and geometrically nonlinear) and further complicated by some loading rate-sensitivity, an hysteretical behaviour, as well a time dependent response under the application of a constant strain (stress-relaxation) or of a constant stress (creep response). In its most pure form, natural rubber has a very low stiffness which makes it susceptible to structural instabilities, such as limit points, bifurcations, and wrinkling (Patil, 2016; Bucchi and Hearn, 2013; Kanner and Horgan, 2007). Instabilities lead to an uncontrolled deformation and ultimately catastrophic failure. This adds to design control challenges as well as excessive material usages. Therefore, one of the major challenges from a material design perspective is to

* Corresponding author.

E-mail addresses: i.c.t.collins@swansea.ac.uk (I. Collins), marco.contino@polimi.it (M. Contino), claudia.marano@polimi.it (C. Marano), i.masters@swansea.ac.uk (I. Masters), mokarram.hossain@swansea.ac.uk (M. Hossain).

<https://doi.org/10.1016/j.euromechsol.2022.104895>

Received 30 October 2022; Received in revised form 1 December 2022; Accepted 9 December 2022

Available online 13 December 2022

0997-7538/© 2022 The Author(s). Published by Elsevier Masson SAS. This is an open access article under the CC BY license (<http://creativecommons.org/licenses/by/4.0/>).

tailor the mechanical properties in accordance with the loading regime without compromising on the advantageous rubber properties. This can be accomplished by using filler particles which are embedded in the polymer matrix, thereby forming a rubber composite. Typical fillers include carbon black and silica, but graphene and carbon nanotubes are also being researched recently (Zhang et al., 2017; Wei et al., 2018). The trade-off for an increase in the mechanical stiffness is accompanied by an increase in the energy dissipation due to interactions between polymer chains and the filler particles. Excessive dissipation is detrimental for energy harvesting since it dampens structural response. Additionally, the fatigue life can be improved or decreased depending on the filler content (Dong et al., 2014). The optimal amount of filler for the stiffness with an acceptable viscoelastic response has not yet been determined for the application of flexible membrane wave energy converters (FlexWECs).

When constructing a structure, it is vital to develop a proper constitutive model to simulate a variety of operation scenarios based on a comprehensive experimental effort to characterise the material. *Hyperelasticity* and *viscous dissipative behaviour* are the two fundamental physical features of rubber-like materials that are of significance. During loading, most rubber-like materials manifest a nonlinear response with a strain-induced softening followed by strain-induced hardening at high strains. At low strains, polymer chains can readily slide over one another, but at higher strains, these chains align, resulting in a more stiff response. In the literature, constitutive models for rubber-like materials are either phenomenological or micromechanical; Steinmann et al. (2012), Marckmann and Verron (2006), Hossain and Steinmann (2013), Hossain et al. (2015) and Dal et al. (2021) provide reviews of various constitutive models. Micro-mechanical models use statistical mechanics based on networks of idealised chain molecules, with real physical characteristics that correspond to mechanical deformation, whereas phenomenological models are based on polynomial functions using strain invariants or principle stretches of strain tensors. Viscous behaviour generated by chain entanglements is defined by time- and rate-dependent features, such as hysteresis during loading–unloading, stress relaxation at a constant strain and stress softening during cyclic loading (Mullins, 1948; Bergström and Boyce, 1998; Miehe and Keck, 2000). To model the time-dependent aspect of stress, an appropriate evolution equation is essential. For finite strain viscoelastic models, two approaches have been used in the literature: integral-based models with stress-like internal variables and differential-based models with strain-like internal variables. The works of Holzapfel (1996), Lion (1997) and Kaliske and Rothert (1997) are some examples of integral-based models; these models are essentially an extension of small strain viscoelasticity. In contrast, differential-based models utilise a multiplicative decomposition of the deformation gradient resulting in an elastic and an inelastic parts for stress and strain variables, as in the works of Lubliner (1985), Simo (1987), Reese and Govindjee (1998) and Bergström and Boyce (1998). These models' parameters are determined through a series of experiments that capture rate-dependent behaviour. Depending on the stress state of the loading regime, the model can be decoupled in an analytical stress formulation for uniaxial, biaxial, or shear stress states. These analytical equations enable straightforward model calibration via a parameter identification procedure. Kleuter et al. (2007), for example, provide a more generic parameter identification framework for finite strain viscoelasticity.

Similar to the development of constitutive models for rubber-like materials, there are concerted efforts to experimentally characterise polymers in order to properly calibrate finite strain models, see Hossain et al. (2012), Liao et al. (2020), Hossain and Liao (2020), Koprowski-Theiß et al. (2011), Johlitz et al. (2010), Zhou et al. (2018), Koprowski-Theiß (2011), Hossain et al. (2020) and Scheffer et al. (2015a). For that, different strain energy functions with nonlinearities, both physical and geometrical, must be considered depending on the polymer's complexity. For instance, Koprowski-Theiß et al. (2011) and Koprowski-Theiß (2011) developed finite strain models of a cellular rubber with

nonlinear viscosity functions while Amin et al. (2006) identified nonlinear dependence of the viscosity in modelling the rate-dependent response of natural and high damping rubbers through an extensive analysis with experimental data obtained from the polymers. Very recently, Hossain et al. (2020) utilised the multiplicative decomposition-based approach with nonlinear evolution equations and nonlinear viscosity functions for an additively manufactured (3D-printed) polymer. In contrast to the works that explored the nonlinear viscosity functions meeting experimental data, Hossain et al. (2012) characterised and calibrated a one-dimensional constitutive model to a highly viscous VHB polymer (3M, USA) using a micromechanically-motivated linear finite strain evolution equation advocated by Linder et al. (2011). To simulate three-dimensional geometries, it is imperative to implement a constitutive model into a finite element framework. Various works have compared models with experimental data and implemented finite viscoelastic models in finite element analysis, Liu et al. (2019), Dipfel et al. (2015), Wang and Chester (2018), Scheffer et al. (2015a) and Behnke et al. (2016). However, there are very limited efforts that demonstrated the implementation of a finite strain viscoelasticity model with nonlinear evolution equations embedded with complex nonlinear viscosity functions. To the best of authors' knowledge, only Scheffer et al. (2015a) and Heng et al. (2021) demonstrated numerical recipes to implement finite strain viscoelastic models with consideration of nonlinear material viscosities. However, none of the aforementioned works are based on analysing rigorous experimental data obtained from polymers that demonstrated both geometrical and material nonlinearities. Hence, *the first aim of our contribution is to develop a viscoelastic model with nonlinear evolution equations and nonlinear viscosity functions followed by its numerical implementation in a finite element framework that are directly derived from experimental data.*

Computational and experimental studies of FlexWECs incorporating polymeric membranes for three-dimensional geometries are limited in the literature. For instance, Moretti et al. (2015) and Rosati Papini et al. (2018) have conducted substantial research on electro-active wave energy converters. Therein, the authors discretise a coupled hyperelastic-electromechanical model for circular and parallelogram membrane geometries that is coupled to the suitable hydrodynamic boundary conditions in a one-dimensional analytical formulation. Chaplin et al. (2012) applied tube distensibility theory for membrane wave energy geometries using tubular membranes. These models are simple with constant elasticity, but do include dissipative effects through a hysteresis parameter. Bucchi and Hearn's (2013) examination of the instability of a tubular geometry employs Ogden and Yeoh's hyperelastic strain energy functions within a commercial finite element package taking finite deformations regime into the modelling framework. Other studies have assumed idealised structural deformations connected to hydrodynamic modelling techniques, see Kurniawan et al. (2017) and Algie et al. (2017). To the best of the authors' knowledge, there is no computational study of flexible materials ideally used in FlexWECs that match time-dependent experimental data with viscoelastic constitutive models. Hence, the second aim of the current manuscript is to perform computational study on FlexWECs taking into account experimentally-derived data obtained from viscoelastic polymers typically used in these devices.

The literature is ubiquitous with studies on natural rubber (Bechir et al., 2006; Kroon, 2010; Carleo et al., 2020; Anand, 1996; Le Saux et al., 2011). As pointed out by Carleo et al. (2020) the majority of previous research works have focused on highly viscoelastic rate-sensitive polymers. Natural rubbers are only rate-sensitive at medium and high strain rates, which can be challenging to characterise under standard test settings. In the current research, an unfilled natural rubber compound that exhibits minimal viscoelasticity and is a suitable material for energy harvesting devices is investigated. In Section 2, a full experimental campaign is conducted, beginning with loading–unloading cyclic uniaxial tensile tests to evaluate the stretchability and hysteresis of the material. Then, using various multi-cyclic loading regimes, the

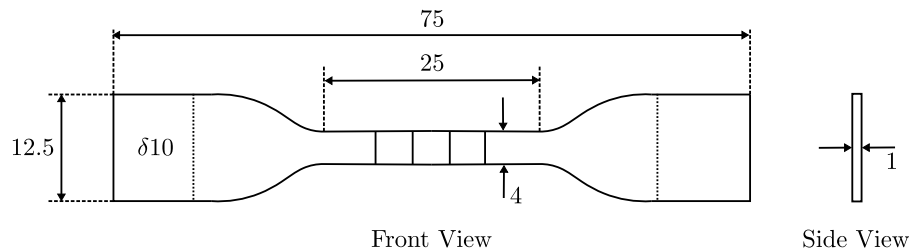


Fig. 1. Dimensions in mm for ISO 37 Sample 2.

levels of stress softening (e.g., Mullins effect) are investigated. The final component of the experiments is devoted to stress relaxation, with various levels of strain considered. In Section 3, the constitutive modelling framework based on the multiplicative decomposition approach is presented, along with a one-dimensional formulation with linearisation for parameter identification. The procedure for the parameter identification is described in Section 4. Section 5 provides the details of the implementation procedure for the material Jacobian in the implicit ABAQUS Standard finite element solver using the ABAQUS UMAT interface. The finite element model is validated against the analytical theory. Section 6 is a case study of a viscoelastic membrane suitable for energy harvesting, whereby the pressure–volume function is evaluated over longer time-scales, as well as cyclic loading conditions which represent real-world loading during energy harvesting.

2. Experimental characterisation of the viscoelastic behaviour

2.1. Specimen preparation

The compounds was first milled at 50 °C in a two-roll milling machine in order to avoid any anisotropy and then cured in a compression moulding press applying a pressure of 9.8 MPa, at 140 °C for 45 min, according to suggestions by the material's supplier. The 1 mm thickness cured sheets were cut with an ISO 37 sample die, where the dimensions are provided in Fig. 1. Each sample was marked with four equally spaced markers on the specimen's gauge length for strain measurements.

2.2. Experimental set-up

Uniaxial tensile tests were performed on an Instron 5967 dynamometer with a load cell of 2 kN, equipped with a pneumatic clamping system. All the tests were video recorded with a 10 megapixel uEye camera UI-5490SE equipped with a photographic lens Nikon 28-105. The video was post-processed using the ImageJ imaging software to evaluate the applied strain: by the ratio between the actual distance between two marks in the gauge length and its value in the undeformed specimen the nominal strain was obtained. All tensile test results are presented as the nominal stress/first Piola–Kirchhoff stress (i.e., the applied force divided by the initial undeformed cross-sectional area) against the nominal strain. The strain rates, mentioned in this contribution, are the time derivative of the nominal strain. The repeatability of the test using different samples influences the reliability of the results. To achieve reproducibility of the test results, more than three samples of each test condition are run, and an averaging technique is used to determine the best data set.

2.3. Stretchability tests

To evaluate stretchability, the sample is stretched until failure. Rubbers can withstand high strains before breaking, Fig. 2 shows the maximum elongation at break for EDS-35. A maximum strain of 744% was reached and a corresponding ultimate tensile strength of 32.8 MPa.

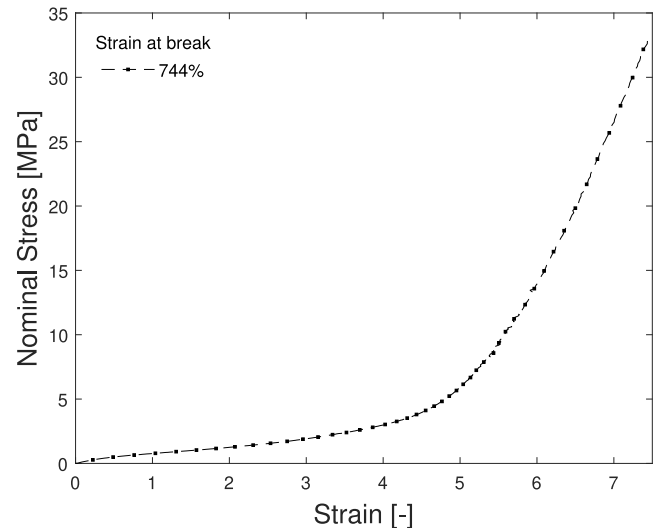
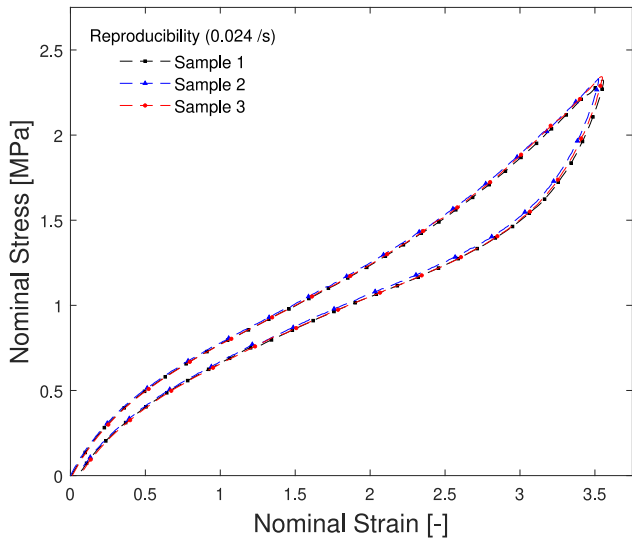


Fig. 2. Stretchability of EDS-35 natural rubber: stress with respect to strain up until the maximum strain of the material.

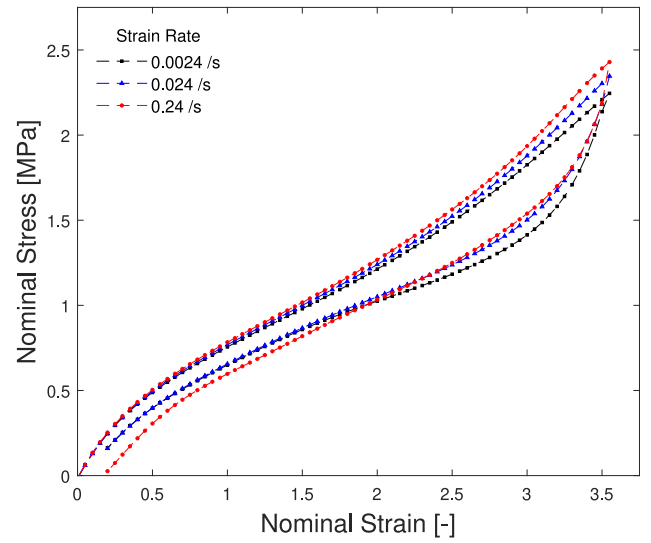
2.4. Loading–unloading cyclic tests

Cyclic tests have been carried out to evaluate the material's hysteretical behaviour and its dependence on the strain rate. The material's dissipative behaviour, as a result of viscoelasticity, observed during the unloading cycle as a reduction in the stress value for the same strain as loading is referred to as *hysteresis*. In this experimental campaign, three displacement rates were employed: 0.1, 1 and 10 mm/s and the last one is close to the maximum displacement rate of the dynamometer. They correspond to strain rates of 0.0024, 0.024, and 0.24/s, respectively. Fig. 3(a) shows the data spread for a loading–unloading experiment at 350% showing excellent repeatability. The rate dependency is shown in Fig. 3(b) which illustrates a minor rate-dependence at room temperature for the studied strain rate range. As reported in literature (Niemczura and Ravi-Chandar, 2011a,b,c; Carleo et al., 2018) the dependence of natural rubber mechanical response on the applied strain rate is significant at strain rates higher than 1.0/s.

To assess the degree of stress-softening exhibited by the rubber-like material, various multi-cycle tests were performed. In Fig. 4(a), a single specimen is stretched 5 times up to of 350%. As shown, the bulk of the stress softening occurs during the first cycle, with subsequent cycles exhibiting little changes in the stress response. In Fig. 4(b), the same specimen is cycled 5 times at 5 strain amplitudes, equating to a total of 25 cycles. For cycles below 200% strains, the softening is negligible, even beyond that value, very little softening is observed. In Fig. 4(c), a more pronounced softening can be observed at strains larger than 400%. The increased hysteretical behaviour is as a result of the so-called strain-induced crystallisation where permanent changes to the micro-structure occurs causing changes to the internal energy of system (Le Cam, 2017; Huneau, 2011). Beyond 450%, the strain hardening

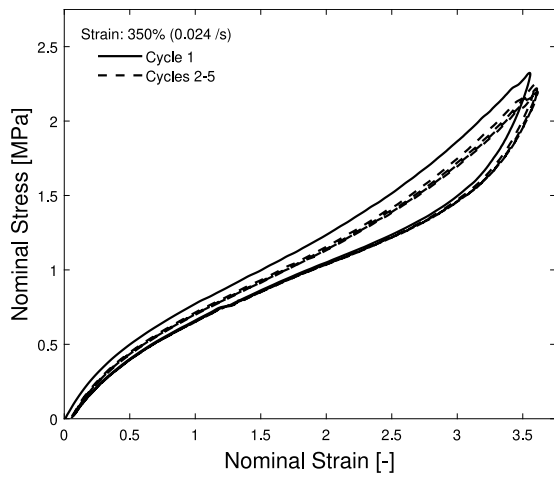


(a) Repeatability test: three different samples at a strain rate of 0.024/s at 350%

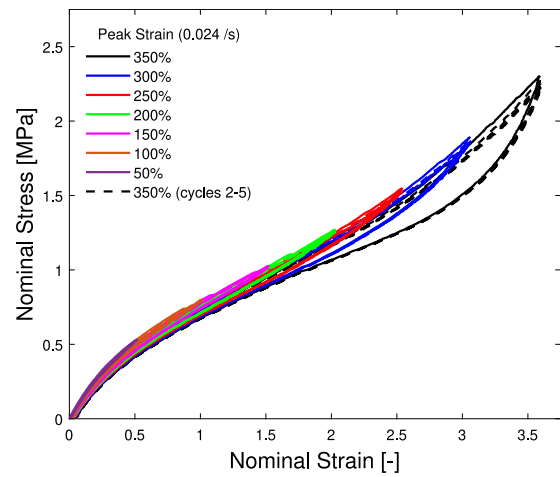


(b) Strain rate-dependency test: three strain rates of 0.24, 0.024 and 0.0024 at 350%

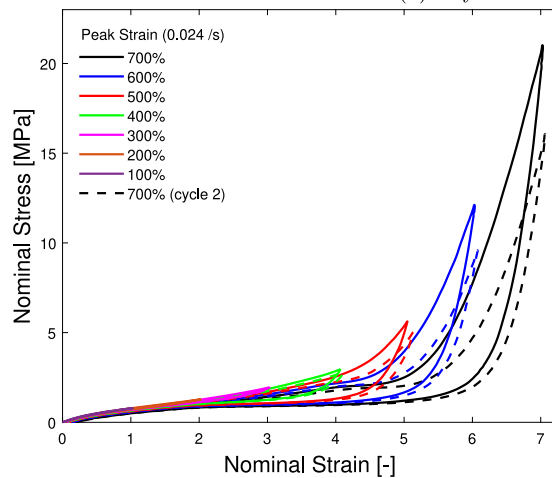
Fig. 3. Single cycle loading–unloading.



(a) 5 cycles at 350 %



(b) 5 cycles at 50-350 % in increments of 50%



(c) 2 cycles at 100-700 % in increments of 100%

Fig. 4. Multi-cycle loading–unloading experiments to quantify stress-softening behaviour.

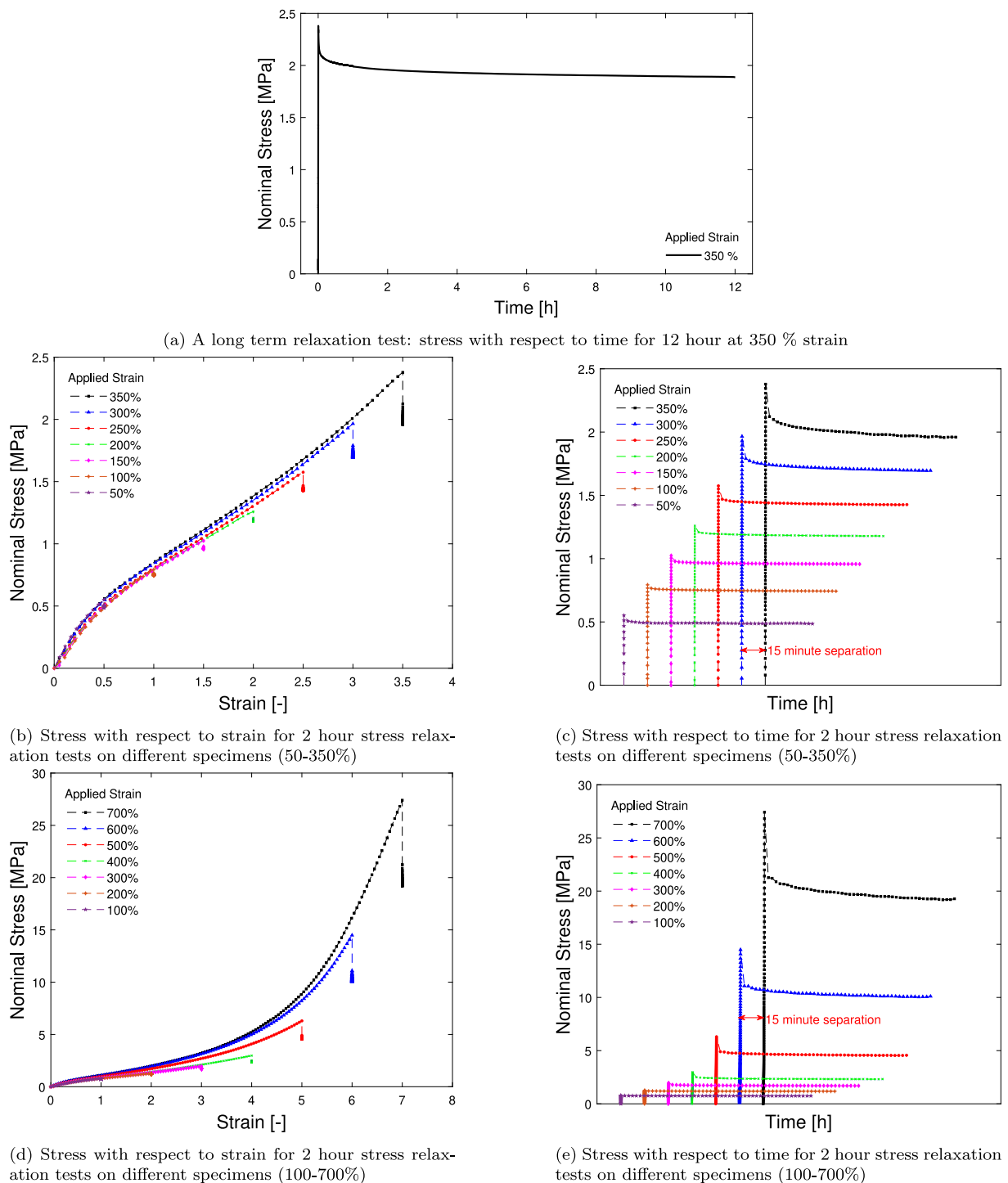


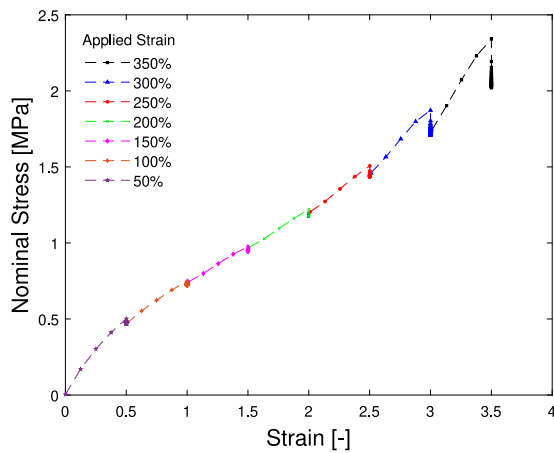
Fig. 5. Single-step stress relaxation experiments, note that stress with respect to time plots are staggered to allow for easier viewing of the overstress.

is also witnessed causing an exponential uptake in the stiffness, as is common with biological tissues (Dal et al., 2022). For the purposes of the application for this characterisation work, the remaining studies are conducted up to 350%.

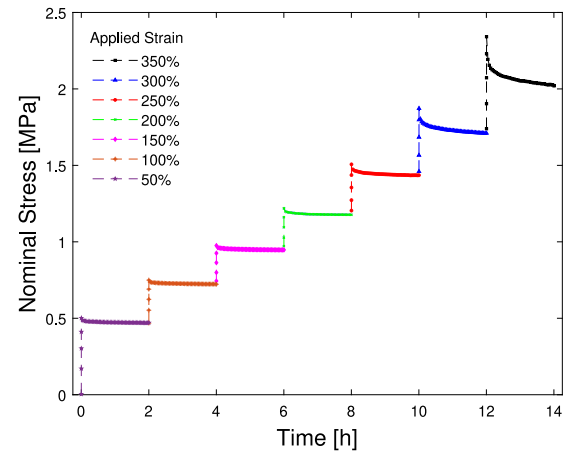
2.5. Stress relaxation tests

When a viscoelastic material is held at a constant strain for a period of time, there is a corresponding reduction in stress until an equilibrium stress is reached, known as the *stress relaxation*. To evaluate this relaxation behaviour, both single-step and multi-step stress relaxation

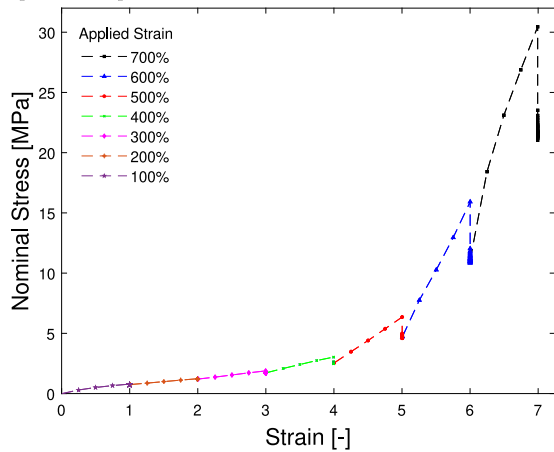
trials were conducted in the literature. In the single-step experiment, the polymeric material is stretched at a very high rate, usually using the machine limit, until the desired strain level is reached where it is held for a period of time. The reduction in load measured in the sample is monitored with respect to time. To grasp an initial understanding of the amount of relaxation exhibited by the material, a twelve hour test was performed at a strain level of 350% as shown in Fig. 5(a). After a period of two hours, the stress relaxed to 82% of the peak value, with a further relaxation to 79% after twelve hours. Relaxation will continue to occur over multiple days, however, most of the stress relaxation happens within first few minutes. Since the change is minimal after



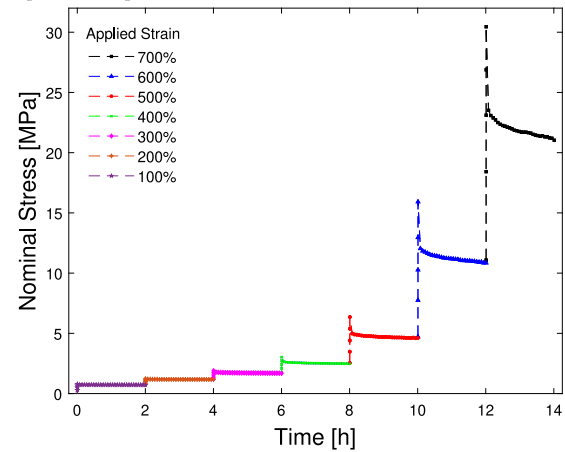
(a) Stress with respect to strain for 2 hour steps on single specimen up to 350%



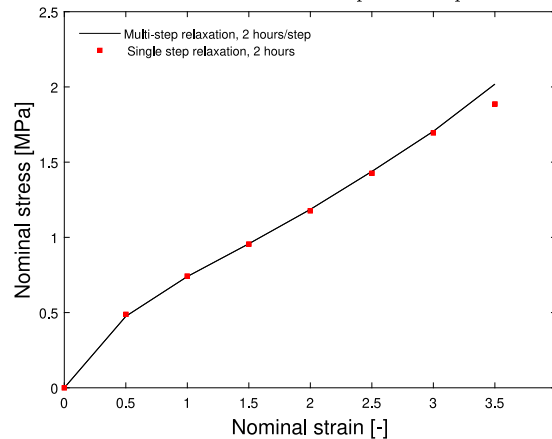
(b) Stress with respect to time for 2 hour steps on single specimen up to 350%



(c) Stress with respect to strain for 2 hour steps on single specimen up to 700%



(d) Stress with respect to time for 2 hour steps on single specimen up to 700%



(e) Stress with respect to strain for equilibrium points

Fig. 6. Multi-step stress relaxation experiments.

the first two hours, the remainder of the relaxation experiments are performed up to two hours. Figs. 5(b) and 5(c) show the stress–strain and stress–time plots for samples up to 350%, while Figs. 5(d) and 5(e) shows these plots for samples up to 700%. For the full range of 100–700% analysed, these equate to imposed deformation of $\epsilon = 1$ and $\epsilon = 7$. The amount of reduction in the overstress (i.e., the difference between the maximum stress and the equilibrium stress) increases with strain amplitude: 6% and 30% for displacements of $\epsilon = 1$ and $\epsilon = 7$,

respectively. However, the bulk of this rise is seen between $\epsilon = 2.5$ (9% decrease) and $\epsilon = 5$ (28% decrease).

In real-world loading, the stress relaxation occurs at multiple times. Therefore, it is essential to evaluate the stress relaxation at multiple strains. To complement the single-step data, a multi-step stress relaxation is performed at the same strain levels and strain rates. The main difference between experiments is the latter is performed only with a single sample which is stretched and held over multiple strains. The material is stretched to the first strain amplitude of 50% and held for

two hours, then is stretched to the next strain amplitude instead of unloading where the process is repeated until the final strain level is reached. Figs. 6(a) and 6(b) show the stress–strain and stress–time plots for up to 350%, while Figs. 6(c) and 6(d) shows these plots for up to 700%. The stress relaxation with respect to time has a similar trend as the single-step relaxation experiments. The stress–strain plot for the relaxed points is compared for single- and multi-step experiments in Fig. 6(e). A good correlation is seen up to 300% which will be used for calibration of the elastic part of the proposed viscoelastic model.

3. Constitutive modelling of viscoelasticity at finite strains

3.1. Kinematics

Rubber-like polymers are as considered as nearly incompressible materials that undergo large deformations without a noticeable change in volume. For modelling rubber-like materials, in finite strain theory, the deformation gradient \mathbf{F} can be decomposed into isochoric (volume preserving) \mathbf{F}_{iso} and volumetric (purely volume change) \mathbf{F}_{vol} components (Bonet and Wood, 1997; Holzapfel, 2000), i.e.,

$$\mathbf{F} = \mathbf{F}_{\text{iso}} \mathbf{F}_{\text{vol}} \quad (1)$$

The isochoric component can further be decomposed into a purely elastic and a viscous parts, cf. Reese and Govindjee (1998, 1997), i.e.,

$$\mathbf{F}_{\text{iso}} = \mathbf{F}_e^j \mathbf{F}_v^j \quad j = 1, \dots, N \quad (2)$$

where j represents the number of Maxwell elements, analogous to small strain viscoelasticity.

3.2. Strain energy function and stress tensors

The multiplicative decomposition of the deformation gradient results in an additive decomposition of the strain energy function. The volumetric strain energy function Ψ_{vol} is represented in a displacement/pressure mixed form to enforce the incompressibility condition, i.e., $\Psi_{\text{vol}} = p(J - 1)$, where p acts as a Lagrange multiplier. The isochoric strain energy is further divided into Ψ_e elastic and Ψ_v viscous representing the elastic and viscous strain energies that are a function of the right Cauchy–Green tensor in which $\mathbf{C} = \mathbf{F}^T \mathbf{F}$. The viscous component is also a function of the multiplicative elastic component of the right Cauchy–Green tensor, $\bar{\mathbf{C}}_e = \mathbf{F}_e^{j,T} \mathbf{F}_e^j$, i.e.,

$$\Psi(\mathbf{C}) = \Psi_{\text{vol}}(J) + \Psi_{\text{iso}}(\bar{\mathbf{C}}); \quad \Psi_{\text{iso}}(\bar{\mathbf{C}}) = \Psi_e(\bar{\mathbf{C}}) + \sum_{j=1}^N \Psi_v(\bar{\mathbf{C}}, \bar{\mathbf{C}}_e^j) \quad (3)$$

Following the dissipation inequality in Reese and Govindjee (1998, 1997), the second Piola–Kirchhoff stress (\mathbf{S}) is decomposed into volumetric, elastic, and viscous components as

$$\mathbf{S} = \mathbf{S}_{\text{vol}} + \mathbf{S}_e + \mathbf{S}_v; \quad \mathbf{S} = -p\mathbf{C}^{-1} + 2 \frac{\partial \Psi_e}{\partial \bar{\mathbf{C}}} + 2 \sum_{j=1}^N \frac{\partial \Psi_v^j}{\partial \bar{\mathbf{C}}} \quad (4)$$

In order to capture the nonlinear curve experimentally observed for the natural rubber under consideration, the elastic strain energy function proposed by Carroll (2010) is chosen since it shows remarkably good performance with a wide range of hyperelastic experimental data (Steinmann et al., 2012). It is a phenomenological model in which both the first and the second invariants of the isochoric right Cauchy–Green tensor are incorporated, i.e.,

$$\Psi_e = a\bar{I}_1 + b\bar{I}_1^4 + c\bar{I}_2^{\frac{1}{2}} \quad (5)$$

where \bar{I}_1 is the first invariant, \bar{I}_2 is the second invariant, while a , b and c are material parameters. The fictitious second Piola–Kirchhoff stress is the derivative of the isochoric strain energy relative to the isochoric Cauchy–Green tensor, i.e., $\bar{\mathbf{S}} = \partial \Psi_{\text{iso}} / \partial \bar{\mathbf{C}}$. The elastic component of the stress is given as

$$\bar{\mathbf{S}}_e = [2a + 8b\bar{I}_1^3] \mathbf{I} + c [\bar{I}_1 \mathbf{I} - \bar{\mathbf{C}}] \bar{I}_2^{-1/2} \quad (6)$$

For the viscous part of the strain energy function, a combination of Yeoh (1993) and neo-Hooke strain energy functions are chosen for the Maxwell elements based on the works of Scheffer et al. (2015a,b) and Hossain et al. (2020).

$$\begin{aligned} \Psi_v(\bar{\mathbf{C}}, \bar{\mathbf{C}}_e^j) &= \sum_{j=1}^N \Psi_v^j = \sum_{j=1}^s \Psi_{\text{yh},v}^j + \sum_{j=s+1}^N \Psi_{\text{nh},v}^j \\ &= \sum_{j=1}^N c_1^j [\bar{I}_{1,e}^j - 3]^3 + \sum_{j=s+1}^N c_2^j [\bar{I}_{1,e}^j - 3] \end{aligned} \quad (7)$$

where c_1^j and c_2^j are the material parameters for the Yeoh and the neo-Hooke strain energy functions, respectively, and $\bar{I}_{1,e}^j$ is the first invariant of $\bar{\mathbf{C}}_e$, i.e., $\bar{I}_{1,e}^j = \text{tr}(\bar{\mathbf{C}}_e) = \text{tr}(\mathbf{F}_v^{j,-T} \dots \bar{\mathbf{C}} \dots \mathbf{F}_v^{j,-1})$. In order to find the viscous component of the stress, i.e., $\bar{\mathbf{S}}_v = 2 \partial \Psi_v / \partial \bar{\mathbf{C}}$, it is necessary to utilise the relationship: $\bar{\mathbf{C}}_e = \mathbf{F}_v^{j,-T} \bar{\mathbf{C}} \mathbf{F}_v^{j,-1}$

$$\bar{\mathbf{S}}_v = 2 \frac{\partial \Psi_v}{\partial \bar{\mathbf{C}}} = \sum_{j=1}^s 6c_1^j [\bar{I}_{1,e}^j - 3]^2 [\mathbf{C}_v^j]^{-1} + \sum_{j=s+1}^N 2c_2^j [\mathbf{C}_v^j]^{-1} \quad (8)$$

Since $\bar{\mathbf{S}}_v$ is a function of \mathbf{C}_v which is a time-dependent parameter, an evolution equation must be required to provide an update of \mathbf{C}_v . A thermodynamically-consistent nonlinear evolution equation is expressed as

$$\dot{\mathbf{C}}_v^j = \frac{4}{\eta^j} \frac{\partial \Psi_{\text{iso}}^j}{\partial \bar{I}_{1,e}^j} \left[\mathbf{C} - \frac{1}{3} [\mathbf{C} : [\mathbf{C}_v^j]^{-1}] \mathbf{C}_v^j \right] \quad (9)$$

Solving $\partial \Psi_{\text{yh},v}^j / \partial \bar{I}_{1,e}^j$ and $\partial \Psi_{\text{nh},v}^j / \partial \bar{I}_{1,e}^j$ results in two evolution equations:

$$\dot{\mathbf{C}}_v^j = \frac{12}{\tau_1^j} [\bar{I}_{1,e}^j - 3]^2 \left[\mathbf{C} - \frac{1}{3} [\mathbf{C} : [\mathbf{C}_v^j]^{-1}] \mathbf{C}_v^j \right], \quad j = 1, \quad \tau_1^j = \frac{\eta^j}{c_1^j} \quad (10)$$

$$\dot{\mathbf{C}}_v^j = \frac{4}{\tau_2^j} \left[\mathbf{C} - \frac{1}{3} [\mathbf{C} : [\mathbf{C}_v^j]^{-1}] \mathbf{C}_v^j \right], \quad j = 2, \dots, N, \quad \tau_2^j = \frac{\eta^j}{c_2^j} \quad (11)$$

With the calculation of $\bar{\mathbf{S}}_v$ defined, the elastic and viscous fictitious stresses are added and converted to isochoric second Piola–Kirchhoff stress through the projection tensor $\mathbb{P} = \mathbb{I} - \frac{1}{3}(\mathbf{C}^{-1} \otimes \mathbf{C}^{-1})$ where $\mathbb{I} = \delta_{ik} \delta_{jl}$ is the fourth order identity tensor. These equations provide the building blocks for any finite element implementation discussed details in Section 5.

$$\bar{\mathbf{S}} = \bar{\mathbf{S}}_e + \bar{\mathbf{S}}_v \Rightarrow \mathbf{S}_{\text{iso}} = J^{-2/3} \mathbb{P} : \bar{\mathbf{S}} \quad (12)$$

Another important element is the so-called tangent operator which is given as the derivative of stress with respect to deformation

$$\mathbb{C} = 2 \frac{\partial \mathbf{S}}{\partial \bar{\mathbf{C}}} = 4 \frac{\partial^2 \Psi}{\partial \bar{\mathbf{C}}^2} \quad (13)$$

due to the complex nature of stress, it is more convenient to perform numerical tangent operation on \mathbf{S} , i.e.,

$$\mathbb{C} = \frac{\mathbf{S}(\mathbf{C} + \Delta \mathbf{C}) - \mathbf{S}(\mathbf{C})}{\Delta \mathbf{C}} \quad (14)$$

The full details of the methodology is provided in Section 5.2.

3.3. One-dimensional formulations of the model

Since the experimental data presented in Section 2 is obtained under uniaxial test conditions, all relevant constitutive equations presented above must be decomposed to one-dimensional forms. It is possible to perform a uniaxial reduction where stretches are applied in only one direction, i.e. $\lambda_1 = \lambda$ and two directions are unhindered. Following the methodology illustrated in Steinmann et al. (2012), Hossain and Steinmann (2013) and Hossain et al. (2015), the first Piola–Kirchhoff stress for the Carroll model is given as

$$P_e = [2a + 8b [2\lambda^{-1} + \lambda^2]^3 + c [1 + 2\lambda^3]^{-1/2}] [\lambda - \lambda^{-2}] \quad (15)$$

For the viscous derivation, to express stress in terms of the eigenvalues λ_e^2 of the elastic Cauchy–Green tensor \mathbf{C}_e , it is convenient to push forward to Cauchy stress through the relationship: $\sigma = P\lambda$. The multiplicative procedure of the deformation gradient results in the eigenvalue relationship of $\lambda^j = \lambda_e^j \lambda_v^j$. The Cauchy stress for the one dimensional model yields

$$\sigma_v = \sum_{j=1}^s c_1^j [2\lambda_e^{-1} + \lambda_e^2 - 3] [\lambda_e^2 - \lambda_e^{-1}] + \sum_{j=s+1}^N c_2^j [\lambda_e^2 - \lambda_e^{-1}] \quad (16)$$

which may be pulled back to the first Piola–Kirchhoff stress for experimental data calibration

$$P_v = \sum_{j=1}^s c_1^j [2\lambda_e^{-1} + \lambda_e^2 - 3] [\lambda_e^2 \lambda^{-1} - [\lambda_e \lambda]^{-1}] + \sum_{j=s+1}^N c_2^j [\lambda_e^2 \lambda^{-1} - [\lambda_e \lambda]^{-1}] \quad (17)$$

The corresponding evolution equations in Eqs. (10) and (11) are written in one-dimensional form through the substitution of $\partial\Psi_v/\partial I_{1,e}$ resulting in

$$\dot{\lambda}_v^j = \frac{4}{\tau^j} \left[\lambda^2 [\lambda_v^j]^{-2} + 2\lambda_v^j \lambda^{-1} - 3 \right]^2 \left[\lambda^2 [\lambda_v^j]^{-1} - [\lambda_v^j]^2 \lambda^{-1} \right], \quad j = 1 \quad (18)$$

$$\dot{\lambda}_v^j = \frac{4}{3\tau^j} \left[\lambda^2 [\lambda_v^j]^{-1} - [\lambda_v^j]^2 \lambda^{-1} \right], \quad j = 2, 3, 4 \quad (19)$$

The internal variable $\dot{\lambda}_v^j$ is the derivative of the viscous stretch with respect to time. Hence, it is necessary to time discretise this equation through an unconditionally stable implicit Euler backward procedure, for Eq. (18) this results in

$$[\lambda_v^j]^{n+1} = [\lambda_v^j]^n + \frac{4}{\tau^j} \left[\lambda^2 [\lambda_v^j]^{-2} + 2\lambda_v^j \lambda^{-1} - 3 \right]^2 \left[\lambda^2 [\lambda_v^j]^{-1} - [\lambda_v^j]^2 \lambda^{-1} \right], \quad (20)$$

where $[\bullet]^k = [\bullet]_{(t_k)}$ and $\Delta t = t_{n+1} - t_n$. This equation is solved through a Newton–Raphson iterative solver in which the first Piola stress is a function of time.

4. Parameter identification and model validation

In this section, the material parameters for the equations in Section 3.3 are identified using the built-in least squares curve fitting function `lsqcurvefit` in Matlab. The identification of material parameters is a multi-step process, firstly the elastic parameters are identified which are then fed into a viscoelastic parameter identification keeping the hyperelastic parameters frozen. The final stage is to validate the model by modifying the strain rate and load range and to compare against a different experimental data-set.

4.1. Elastic material parameter identification

The goal of an elastic parameter identification is to remove the viscoelastic effects from the material and to capture only the elastic behaviour. This can be achieved through finding the fully relaxed equilibrium points of the material. There are three possible methodologies: (1) relaxed points from a single-step stress relaxation, (2) relaxed points from a multi-step stress relaxation, or (3) monotonic quasi-static loading, i.e. loading at an extremely slow strain rate, see Amin et al. (2006), Johlitz et al. (2007) and Hossain et al. (2012). Herein, the data is fitted using multi-step relaxation experiments. As mentioned earlier, to capture the nonlinear response of the natural rubber, the Carroll hyperelastic model is chosen since it offers excellent modelling capabilities of most rubber-like materials at very large strains (Steinmann et al., 2012; Hossain and Steinmann, 2013). The elastic fit is shown in Fig. 7(a) showing close alignment to all the data points. The identified elastic parameters a, b and c are given in Table 1.

Table 1

Elastic parameters identified using equilibrium data only.

a [MPa]	b [MPa]	c [MPa]
0.19	2.9×10^{-7}	0.17

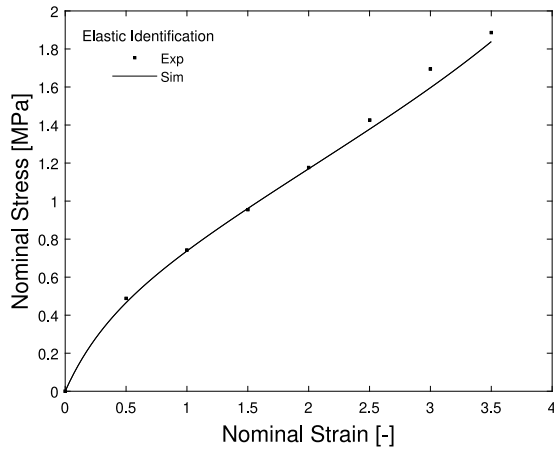
4.2. Viscoelastic material parameter identification

The remaining time-dependent viscoelastic parameters c_1^j , c_2^j , and τ^j need to be identified. For that, a strain of 350% was chosen since it shows the nonlinear response whilst not reaching the exponential hardening phase as shown in Fig. 4(c). The viscous fitting procedure uses the previously identified elastic parameters. The viscous time-dependent parameters are then identified through a fitting procedure which evaluates different coefficient values until the fitting tolerance is reached. For the first fitting, constant values of τ^1 and τ^2 were chosen. The model failed to capture an accurate response beyond 150% strains, due to nonlinearity of the viscosity at higher strain values. Therefore, a nonlinear function was introduced for the Yeoh component of the model shown in Eq. (21). The Frobenius norm of the deformation tensor $\|\mathbf{D}\|$ multiplied by trace of the Cauchy–Green tensor \mathbf{C} results in an uptake in the viscosity as the strain evolves. With this function introduced, the model was able to capture a single strain rate of 0.24/s successfully. It is noted that the number of Maxwell elements required is a ‘trial and error’ process until a desirable fit is achieved. Since this material has relatively low hysteretic behaviour, it was found that one Yeoh and one neo-Hooke elements were sufficient to adequately capture the material dissipation. This model was validated against two other strain-rates of 0.024 and 0.0024/s as illustrated in Fig. 7(b). The model was not able to capture these lower strain-rates, it is speculated due to the low strain-rate dependency, the parameters are sensitive to the Δt value. Therefore, another nonlinear parameter τ_{13} is embedded in Eq. (21). An exponential function utilising the Frobenius norm of the rate of change of the deformation gradient $\|\dot{\mathbf{F}}\|$ acts as a compensation parameter for this low strain rate dependency. To identify the k coefficients, a logistic regression analysis was performed whereby several τ_{13} values were modified at different strain rates to achieve the desired material response, shown in Fig. 8(a). The resulting viscosity is both stretch level and strain rate-dependent which is shown in Fig. 8(b). The neo-Hookean τ^2 parameter was kept constant as it modifies the dissipation below 150% and having minimal effect on high strain behaviour. The model was then simultaneously run at three strain levels resulting in a reasonable fitting with experimental data as shown in Fig. 8(c). As the viscoelasticity is minimal, i.e. the rate-dependency, for the case of this material, achieving a good fit with the experimental data is challenging. The strain-rate compensation parameter τ_{13} introduced here does give reasonable results for strain values between 10^{-5} and 1/s. The correlation could be improved by incorporating additional nonlinear parameters in the τ_1^1 function. Note that the viscoelastic compensation could not be increased beyond a certain threshold due to unstable numerical values with respect to strain rate. Performing the parameter identification at lower strain levels would ensure an easier fitting process, however the model would then only be validated for this lower strain level range. All the model parameters are given in Table 2. Finally, the nonlinear viscosity functions are given as

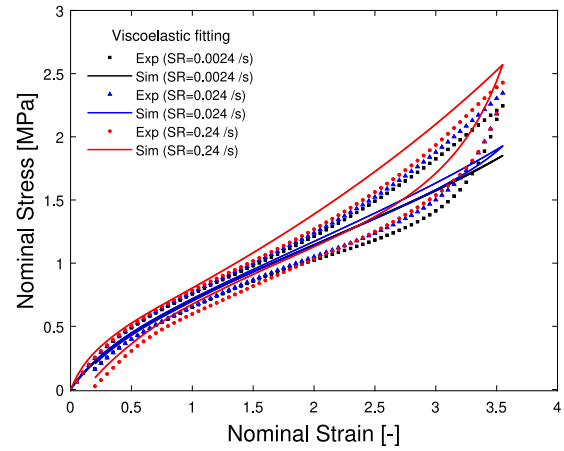
$$\begin{aligned} \tau_1^1 &= \tau_{11} + [\tau_{12} + \tau_{13} \exp(-k_{13} \|\mathbf{D}\|)] [\text{tr}\mathbf{C} - 3]^2, \\ \tau_{13} &= k_{12} \exp(-k_{13} \|\dot{\mathbf{F}}\|) + k_{14} \exp(-k_{15} \|\dot{\mathbf{F}}\|) + k_{16} \exp(-k_{17} \|\dot{\mathbf{F}}\|) \\ &\quad + k_{16} \exp(-k_{17} \|\dot{\mathbf{F}}\|) \end{aligned} \quad (21)$$

which, in the case of uniaxial deformation, result in

$$\begin{aligned} \tau_1^1 &= \tau_{11} + [\tau_{12} + \tau_{13} \exp(-k_{11} \dot{\lambda}/\lambda)] [\lambda^2 + 2\lambda^{-1} - 3]^2, \\ \tau_{13} &= k_{12} \exp(-k_{13} |\dot{\lambda}|) + k_{14} \exp(-k_{15} |\dot{\lambda}|) + k_{16} \exp(-k_{17} |\dot{\lambda}|) \\ &\quad + k_{16} \exp(-k_{17} |\dot{\lambda}|) \end{aligned} \quad (22)$$

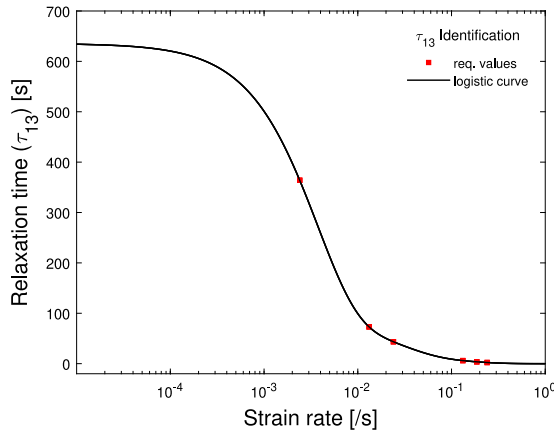


(a) Elastic parameter identification up to 350 % strain

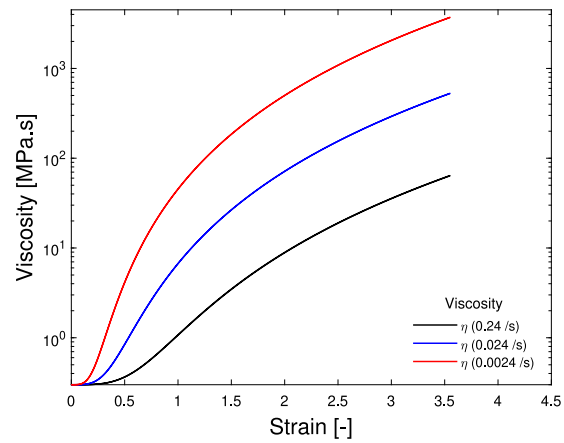


(b) Viscoelastic parameter identification for three different strain rates at 350 % strain

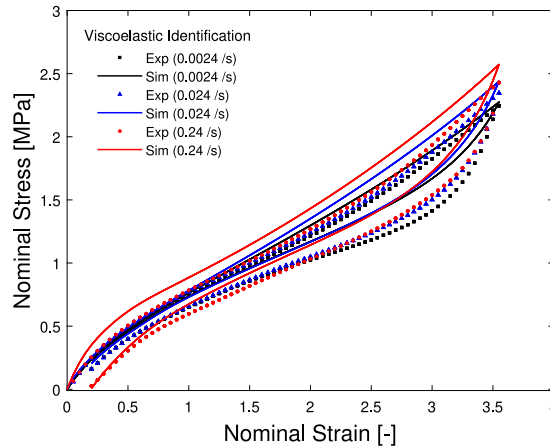
Fig. 7. Parameter identification for elastic and viscoelastic models using constant τ_{13} value.



(a) Identification of k coefficients for nonlinear τ_{13} , where the red squares represent the required compensation values to minimise rate dependency for a strain rate range of 10^{-5} to 1 /s



(b) Three different strain rates for the nonlinear viscosity based on the relaxation parameter in Eq. 22



(c) Viscoelastic validation at three different strain rates of 350 % with nonlinear τ_{13}

Fig. 8. Nonlinear viscosity parameter identification using strain rate-dependent data.

4.3. Model validation: loading–unloading data

The material parameters identification procedure illustrated in Sections 4.1 and 4.2 are based on strain values of 350%. The model is now

validated at different strains values to understand the accuracy over a range of loading regimes. The strain-hardening phase occurs at strains above 200%. The goal of the validation was to see if the model was able to adequately capture the behaviour in the strain-softening phase

Table 2
Viscous parameters identified using strain rate-dependent data.

c_1 [MPa]	τ_{11} [s]	τ_{12} [s]	k_{11} [s]	k_{12} [s]	k_{13} [s]
3×10^{-2}	10	3	0.1	72.04	37.88
k_{14} [s]	k_{15} [s]	k_{16} [s]	k_{17} [s]	c_3 [MPa]	τ^2 [s]
546.8	276.3	8.393	8.297	2×10^{-1}	4

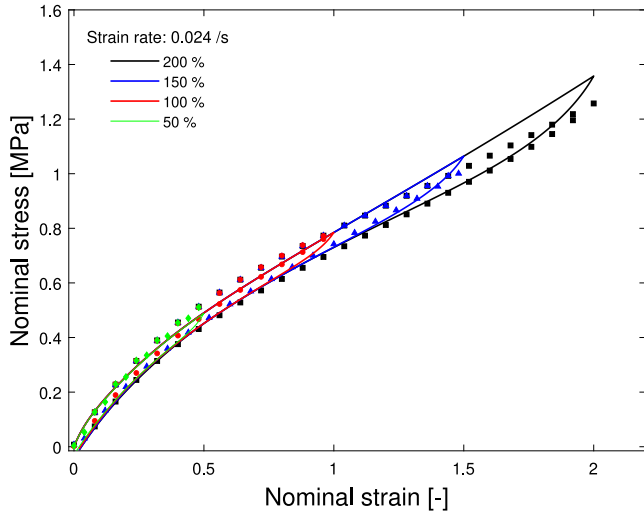
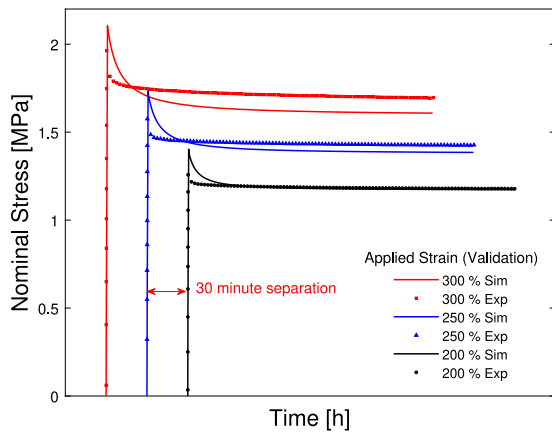


Fig. 9. Viscoelastic model validation at four strain levels between 50%–200% at strain rate of 0.024/s.

at relatively lower strains. Fig. 9 shows the validation of four different strain levels: 50, 100, 150 and 200% at a strain rate of 0.024/s, showing good correlation. The goodness of fit for all strain ranges and rates investigated is shown in Table 3. It is shown that the model performs best at intermediate strain rates and strains, i.e. 0.024/s and 100%–200%. Outside of these values the goodness of fit reduces, although still performs reasonably well.

4.4. Model validation: stress relaxation data

Another form of validation is through the stress relaxation experiments. Six strain amplitudes are validated from 50% to 300%, these are given in Figs. 10(a) and 10(b). The model shows a good correlation for low strain amplitudes, however the accuracy decrease beyond 150%; witnessed as an over-estimation in the overstress and equilibrium point.



(a) Validation at 200, 250 and 300 %

Table 3
Goodness of fit (R^2) for strain ranges and rates investigated during an loading–unloading simulation.

Strain range [-]	Strain rate [/s]	R^2
50	0.024	0.9344
100	0.024	0.9841
150	0.024	0.9951
200	0.024	0.9907
350	{0.0024, 0.024, 0.24}	{0.9513, 0.9647, 0.9568}

Table 4
Goodness of fit (R^2) for 6 strain levels during stress relaxation simulations.

Strain level [-]	R^2
50	0.7871
100	0.8549
150	0.9243
200	0.9378
250	0.9298
300	0.8851

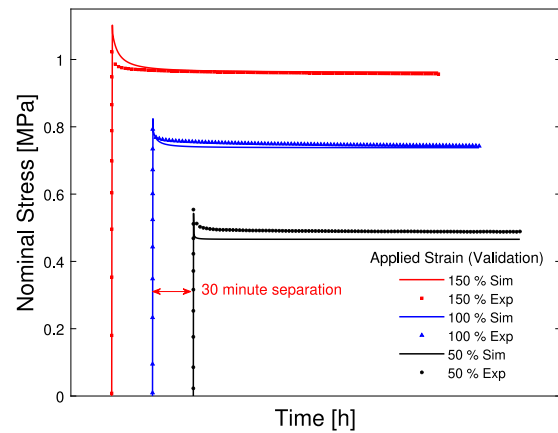
The goodness of fit is shown in Table 4, like the loading–unloading experiments, the optimum model range is at the intermediate strain levels of 100%–200%.

5. Finite element implementation

The constitutive equations presented in Section 3 have now been incorporated into a commercial finite element solver for the solving of three-dimensional geometries. Since the one-dimensional simplifications in Section 4 no longer apply, calculating the non-linear evolution equation that does not have any closed-form (analytical) solution is one of the more difficult aspects of incorporating it in the finite element method; a technique overview is provided in Section 5.1. As this model is solved numerically, the resulting stress and stiffness matrices must therefore be numerically determined. The user is responsible for providing ABAQUS UMAT with the spatial stress and Jacobian update with the method given in Section 5.2. This numerical implementation must be validated against analytical formulations in order to ensure its accuracy. Hence three strain rates are validated against the analytical simulations in Section 5.3.

5.1. Solving the evolution equation

The key aspect of a viscoelastic model is the viscous stress contribution S_v which is dependent on the viscous Cauchy–Green tensor C_v^j . As shown in Eqs. (10) and (11), the calculation C_v^j requires time



(b) Validation at 50, 100 and 150 %

Fig. 10. Single-step stress relaxation for 2 h model validation.

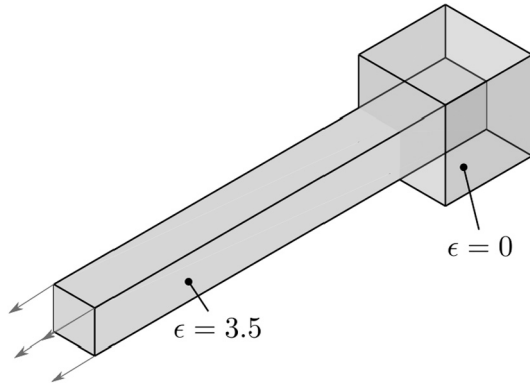


Fig. 11. Single element uniaxial boundary condition; initial and maximum deformation shown.

discretisation; therefore a suitable mechanism for updating these evolution equations must be proposed. In Scheffer et al. (2015a), the unconditionally stable Euler backward method (EBM) is utilised at each (Gauss) integration point to solve the evolution equation. The computational cost of running Newton–Raphson iterations involving fourth and second order tensors is the major downside of this method. There have been proposed solutions to simplify the issue. For instance, Shutov et al. (2013) considered the uni-modularity of tensors, which enables the closed-form representations of evolution equations. However, that effort was successful only for simple evolution equations resulting from neo-Hookean-type energy functions appearing in the viscous part of the total energy function. A similar technique is further applied by Landgraf et al. (2015) in an effort to obtain a more sophisticated generalised evolution equation containing first invariant components. They showed it is possible to reduce the model to a single scalar Newton–Raphson process. However, the approach devised by Landgraf et al. (2015) is not implemented into a finite element solver. Hence, the current study extended the method of Landgraf et al. (2015) into ABAQUS UMAT, enabling the selection of any first invariant-based viscoelastic model for complex polymer viscoelasticity at a minimal computational cost without involving complicated fourth and second order tensors' calculations at every Gauss point. Ultimately, this yields a versatile viscoelastic framework which can utilise any highly nonlinear evolution functions. Using similar notation, the unimodularity of a tensor is defined as $\bar{\mathbf{A}} = (\det(\mathbf{A}))^{-1/3} \mathbf{A}$. The update for $[\mathbf{C}_v^j]^{n+1}$ is set as equal to the Euler backward method unimodular tensor $[\mathbf{C}_v^j]_{EBM}^{n+1}$, resulting

in

$$[\mathbf{C}_v^j]^{n+1} = \overline{[\mathbf{C}_v^j]_{EBM}^{n+1}} = \left(\det([\mathbf{C}_v^j]_{EBM}^{n+1}) \right)^{-1/3} [\mathbf{C}_v^j]_{EBM}^{n+1} \quad (23)$$

Now consider applying the Euler backward method to Eq. (9) and substitution into Eq. (23) which yields

$$[\mathbf{C}_v^j]_{EBM}^{n+1} = [\mathbf{C}_v^j]^n + \left\{ \frac{4\Delta t}{\eta^j} \frac{\partial \Psi_v}{\partial \bar{\mathbf{I}}_{1e}} \left[\bar{\mathbf{C}} - \frac{1}{3} \text{tr}([\mathbf{C}_v^j]^{-1} \cdot \bar{\mathbf{C}}) \bar{\mathbf{C}} \right] \right\}^{n+1} \quad (24)$$

As is shown in Shutov et al. (2013), Eq. (24) can be rearranged such that $[\mathbf{C}_v^j]_{EBM}^{n+1}$ is removed from the right hand side (RHS) of Eq. (24), allowing for the expression

$$\overline{[\mathbf{C}_v^j]^{n+1}} = \overline{[\mathbf{C}_v^j]^n + \left\{ \frac{4\Delta t}{\eta^j} \frac{\partial \Psi_v}{\partial \bar{\mathbf{I}}_{1e}} \bar{\mathbf{C}} \right\}^{n+1}} \quad (25)$$

where the overline definition $\overline{(\cdot)}$ is expressed in Eq. (23). If the derivatives of $\partial \Psi_{nh,v}^j / \partial \bar{\mathbf{I}}_{1e}$ and $\partial \Psi_{yh,v}^j / \partial \bar{\mathbf{I}}_{1e}$ are substituted in Eq. (25), this results in two time discretised evolution equations, where neo-Hooke is

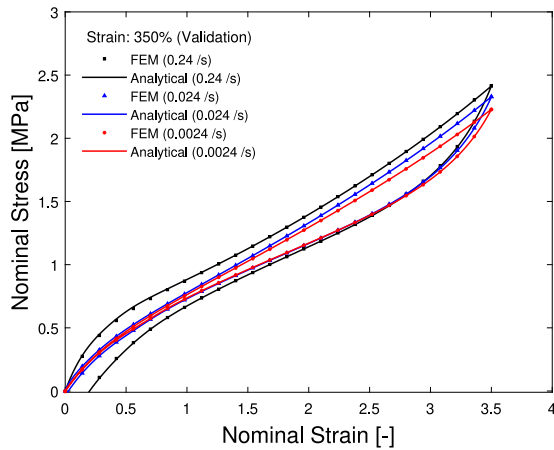
$$[\mathbf{C}_v^j]^{n+1} = [\mathbf{C}_v^j]^n + \left\{ \frac{4\Delta t c_2}{\eta^j} \bar{\mathbf{C}} \right\}^{n+1} = \overline{[\mathbf{C}_v^j]^n + \left\{ \frac{4\Delta t}{\tau^j} \bar{\mathbf{C}} \right\}^{n+1}} \quad (26)$$

which can be solved in a single step. Now consider the Yeoh energy function that can be written as

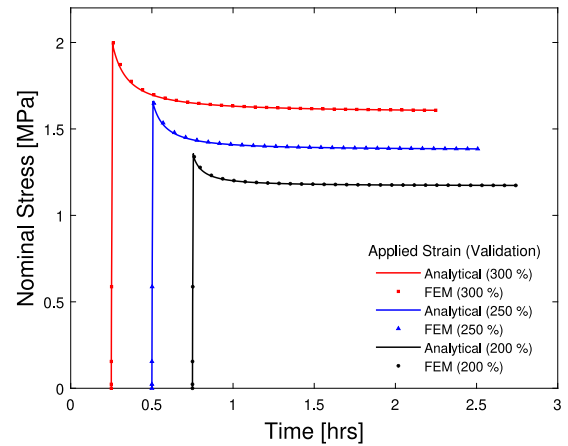
$$\begin{aligned} [\mathbf{C}_v^j]^{n+1} &= \overline{[\mathbf{C}_v^j]^n + \left\{ \frac{12\Delta t c_1 (I_{1e}^j - 3)^2}{\eta^j} \bar{\mathbf{C}} \right\}^{n+1}} \\ &= \overline{[\mathbf{C}_v^j]^n + \left\{ \frac{12\Delta t (I_{1e}^j - 3)^2}{\tau^j} \bar{\mathbf{C}} \right\}^{n+1}} \end{aligned} \quad (27)$$

Since I_{1e}^j is dependent on \mathbf{C}_v^j , it is necessary to perform some Newton–Raphson iterations of this scalar term to solve. If one is to consider that $\bar{\mathbf{I}}_{1e}^j = \mathbf{I} : \bar{\mathbf{C}}_e$, then through some algebra given in Liu et al. (2019), it is possible to show that $\bar{\mathbf{I}}_{1e}^j = \bar{\mathbf{C}} : \mathbf{C}_v^j$. With that definition, taking the inverse of $[\mathbf{C}_v^j]^{n+1}$ and performing the double contraction with respect to $\bar{\mathbf{C}}$ on both sides of Eq. (27) yields

$$[\mathbf{I}_{1e}^j]^{n+1} = \left[[\mathbf{C}_v^j]^n + \left\{ \frac{6\Delta t (I_{1e}^j - 3)^2}{\tau^j} \bar{\mathbf{C}} \right\}^{n+1} \right]^{-1} : \bar{\mathbf{C}}^{n+1} \quad (28)$$



(a) Loading-unloading at 350 % with three strain rates



(b) Stress relaxation for three initial strain amplitudes

Fig. 12. Finite element implementation validation against analytical model prediction.

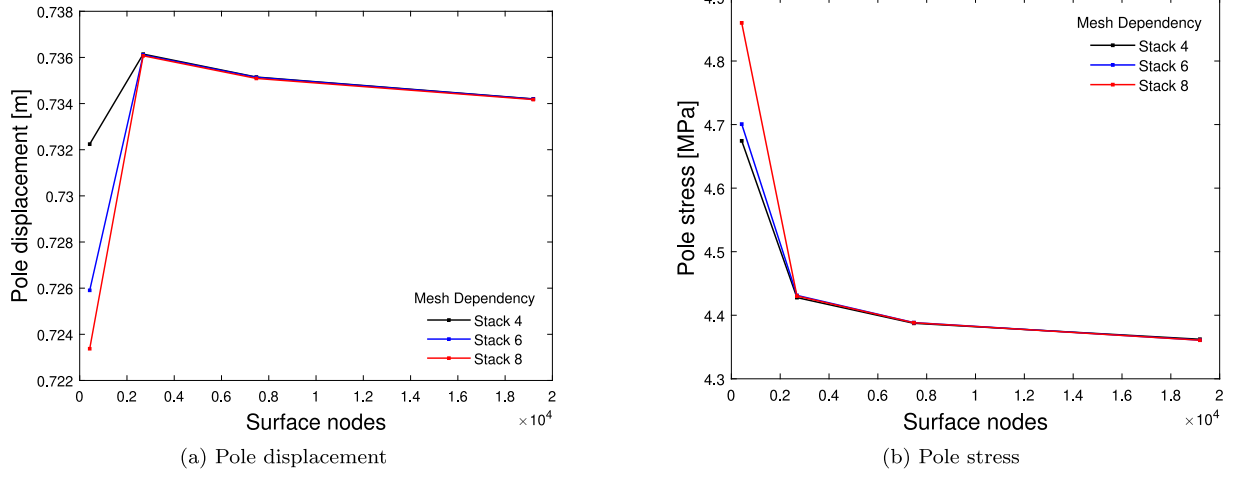


Fig. 13. Mesh refinement results using 4 surface element and 3 stack combinations. The results are based on the pole displacement and stress, where the pole is referred to the centre point of the membrane in the initial configuration.

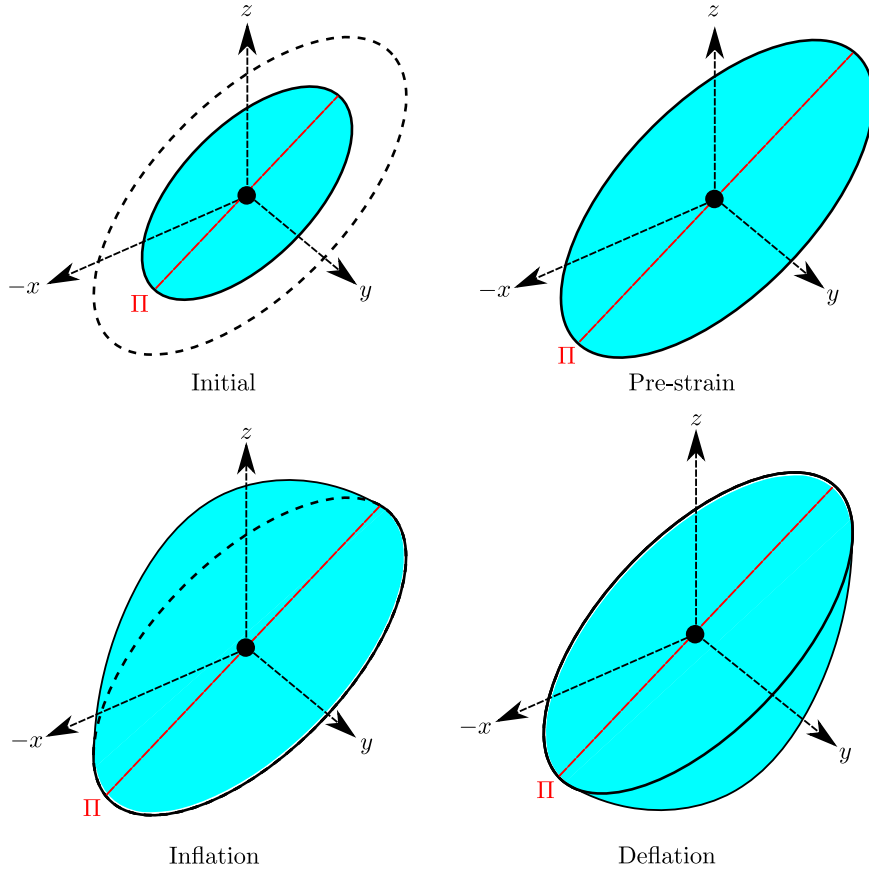


Fig. 14. Boundary conditions for a circular disc membrane, showing the coordinate system and Π spline used in the following figures. y is in the plane of the membrane, Π is in the xz vertical plane.

Eq. (28) can be solved through the function

$$\begin{aligned}
 f\left([I_{1e}^j]^{n+1}\right) &= [I_{1e}^j]^{n+1} - \left[[C_v^j]^n + \left\{ \frac{6\Delta t(I_{1e}^j - 3)^2}{\tau^j} \bar{C} \right\}^{n+1} \right]^{-1} : \bar{C}^{n+1} \\
 &= [I_{1e}^j]^{n+1} - \left[\left(\det([C_v^j]_{EBM}^{n+1}) \right)^{-1/3} [C_v^j]_{EBM}^{n+1} \right]^{-1} : \bar{C}^{n+1}
 \end{aligned}
 \tag{29}$$

with a new update for $[I_{1e}^j]_*^{n+1}$, Eq. (27) can be directly updated through a substitution.

5.2. Stress and tangent operators update

The total fictitious stress is summed and converted to isochoric stress in Eq. (12), then the volumetric stress is added in Eq. (4). For ABAQUS Standard, the stress has to be provided as a Cauchy stress in Voigt notation σ_{voigt} and the material Jacobian in a Jaumann format

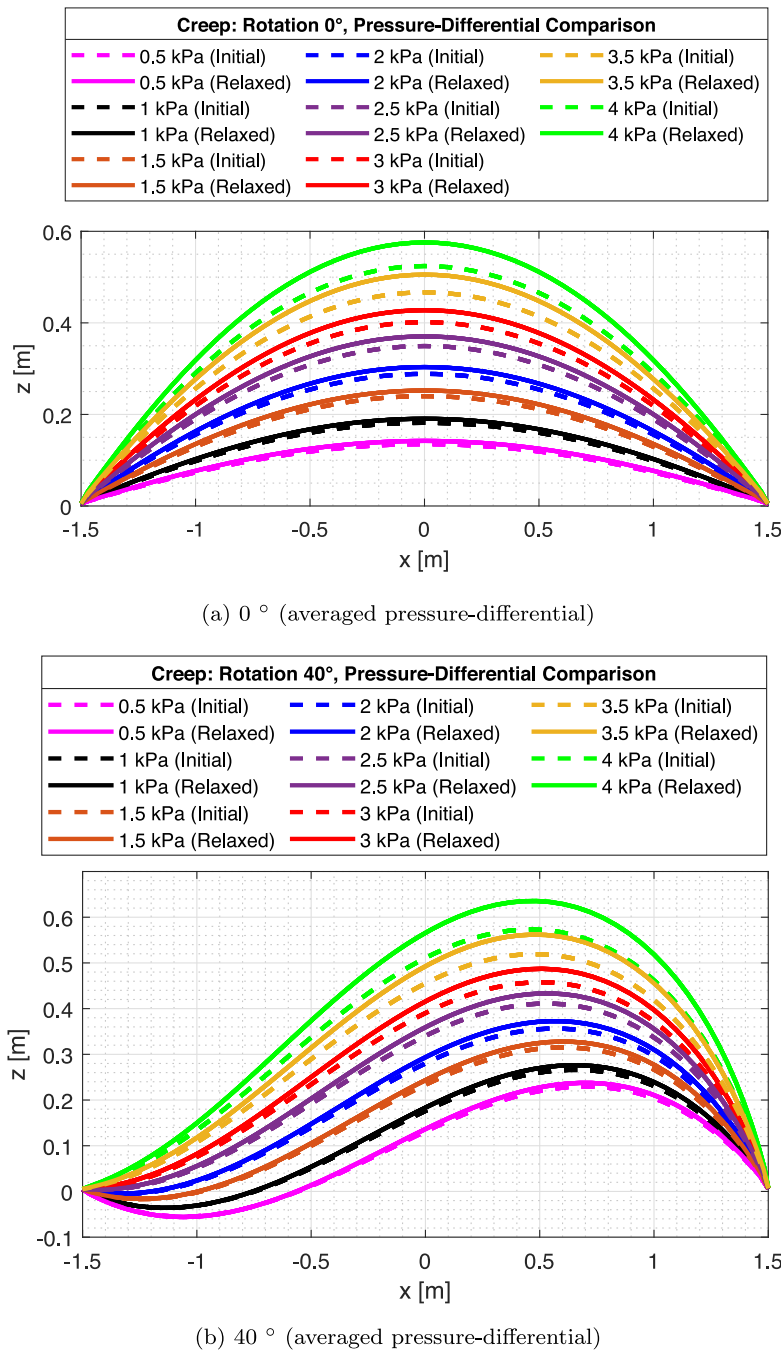


Fig. 15. The influence of membrane orientation on the membrane shape and creep behaviour after two hours.

$\nabla_{\mathbb{C}}$. The second Piola–Kirchhoff stress is converted to the Cauchy stress using the following relation

$$\sigma = J^{-1} \mathbf{F} \mathbf{S} \mathbf{F}^T \quad (30)$$

As per the procedure proposed in Miehe (1996), the calculation of a numerical tangent by perturbing the deformation gradient is

$$\mathbf{F}^{\epsilon(kl)} = \mathbf{F} + \frac{\epsilon}{2} [e_k \otimes e_l \mathbf{F} + e_l \otimes e_k \mathbf{F}], \quad \epsilon = 1 \times 10^{-10} \quad (31)$$

The Kirchhoff stress is calculated with and without perturbation

$$\tau^{\epsilon(kl)}(\mathbf{F}^{\epsilon(kl)}) = J^{\epsilon(kl)} \sigma^{\epsilon(kl)}, \quad \tau(\mathbf{F}) = J \sigma \quad (32)$$

The spatial Jaumann tangent moduli as per the requirement for an ABAQUS UMAT is then calculated as

$$\nabla_{\mathbb{C}} = \frac{1}{J \epsilon} [\tau^{\epsilon(kl)}(\mathbf{F}^{\epsilon(kl)}) - \tau(\mathbf{F})] \quad (33)$$

5.3. Finite element implementation validation

The finite element implementation was validated using a single element uniaxial test condition with the same input material parameters as in the analytical model, see Fig. 11 for the deformed and undeformed states of the element. The model was validated at three different strains rates in a loading–unloading test, and comparison to the analytical model is shown in Fig. 12(a). Additionally, three stress relaxations tests were performed, shown in Fig. 12(b). Both test confirmed successful

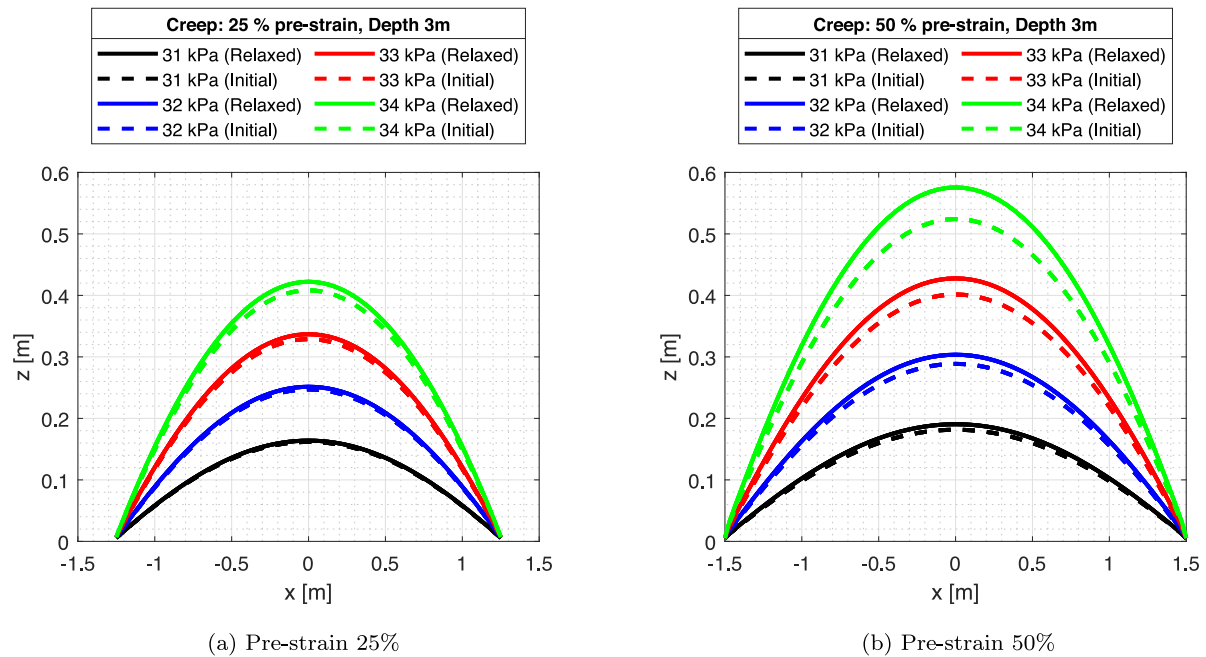


Fig. 16. The influence of membrane pre-strain on the creep behaviour after two hours.

implementation of the model in an ABAQUS UMAT resulting in an excellent correlation with analytical forms.

6. Pneumatic cell FlexWEC case study

The pneumatic cell was selected as a case study after evaluating the categorisation for flexible wave energy converters offered by Collins et al. (2021). The response of a flexible membrane is a fairly complex issue with various nonlinear features, including anisotropy and biaxial behaviour of the membrane material. As a result, an idealised quasi-static analysis of a circular membrane was selected and assessed under various loading circumstances anticipated during operation, including long-term creep and cyclic loading. This work's objective was not to mimic the high-fidelity fluid–structure interaction that happens during operating conditions, but rather to examine the influence of the nonlinear transient features resulting from viscoelastic dissipation on the pressure–volume function of the membrane. Future works will consider the high fidelity fluid–structure interaction with the possibility of coupling to the viscous dissipative membrane.

6.1. Boundary conditions

An idealised circular membrane was chosen and evaluated under various loading conditions expected during its operation. The membrane is one metre in diameter with a thickness of ten centimetres. The global boundary conditions applied to the membrane are shown in Fig. 14. For the case studies conducted in this paper, the membrane is rotated 40° relative to the x -axis, resulting in a non-uniform pressure-loading distribution. Then a pre-strain is applied to the membrane. In order to avoid any significant stress concentrations, a fictitious clamp boundary condition is proposed, whereby the membrane is bonded to a rigid material which has rotational degrees of freedom. The internal air and external hydrostatic pressures are applied simultaneously to each side of the membrane surface where the pressure-differential is kept to a minimum. The membrane is inflated and deflated by increasing and decreasing the internal air pressure. The membrane spline II is used for figures in Sections 6.2 and 6.3. The material modelling framework was implemented for continuum based element problems since it offers

the best flexibility for performing the analysis. The drawbacks of these elements is the potential for artificial shear locking in large bending problems. Therefore it is necessary to perform a mesh refinement study. Due to the near incompressibility, i.e. $\nu \approx 0.5$, the hybrid element C3D8H is considered since it includes an additional degree of freedom that determines the pressure stress in the element directly (Abaqus, 2014). Since the studied problem is under plane stress conditions, the optimum element would be a shell/membrane element, see Fehervary et al. (2020) for details on UMAT implementation. However, due to the greater flexibility for solving different analyses, the full three-dimensional UMAT implementation is considered here. An automatic mesh refinement algorithm was created in Python to change the number of seeds at each partition of the membrane. Two parameters were modified: the number of surface elements and the number of elements in the thickness direction. Refer to Fig. 13 in for the results of the mesh refinement study.

6.2. Creep test

If a membrane is inflated and maintained at a constant pressure, the creep will over time. Using these simulations, the influence of viscoelasticity on the long-term pressure–volume (P–V) function is simulated. During these simulations, four independent variables were altered: the orientation of the membrane, the submersion depth, the amount of pre-strain applied, and the viscoelastic characteristics of the membrane material. Using various submersion depths and orientations, the effect of the pressure differential across the membrane surface is explored. Below is a summary of the conclusions from these simulations.

6.2.1. Influence of boundary conditions

Three membrane orientations at a depth of one and three metres are compared; with internal pressures ranging from 11–15 kPa and 31–36 kPa, respectively. The averaged positive pressure-differential for the inflation of these analyses is given in Fig. 15. Due to the equal hydrostatic pressure acting on the membrane surface, the inflation is fully symmetric for orientation 0° . As the membrane is rotated around its centre, the non-uniform hydrostatic pressure alters the membrane's shape. As demonstrated in Fig. 15b for 40° , when a greater pressure

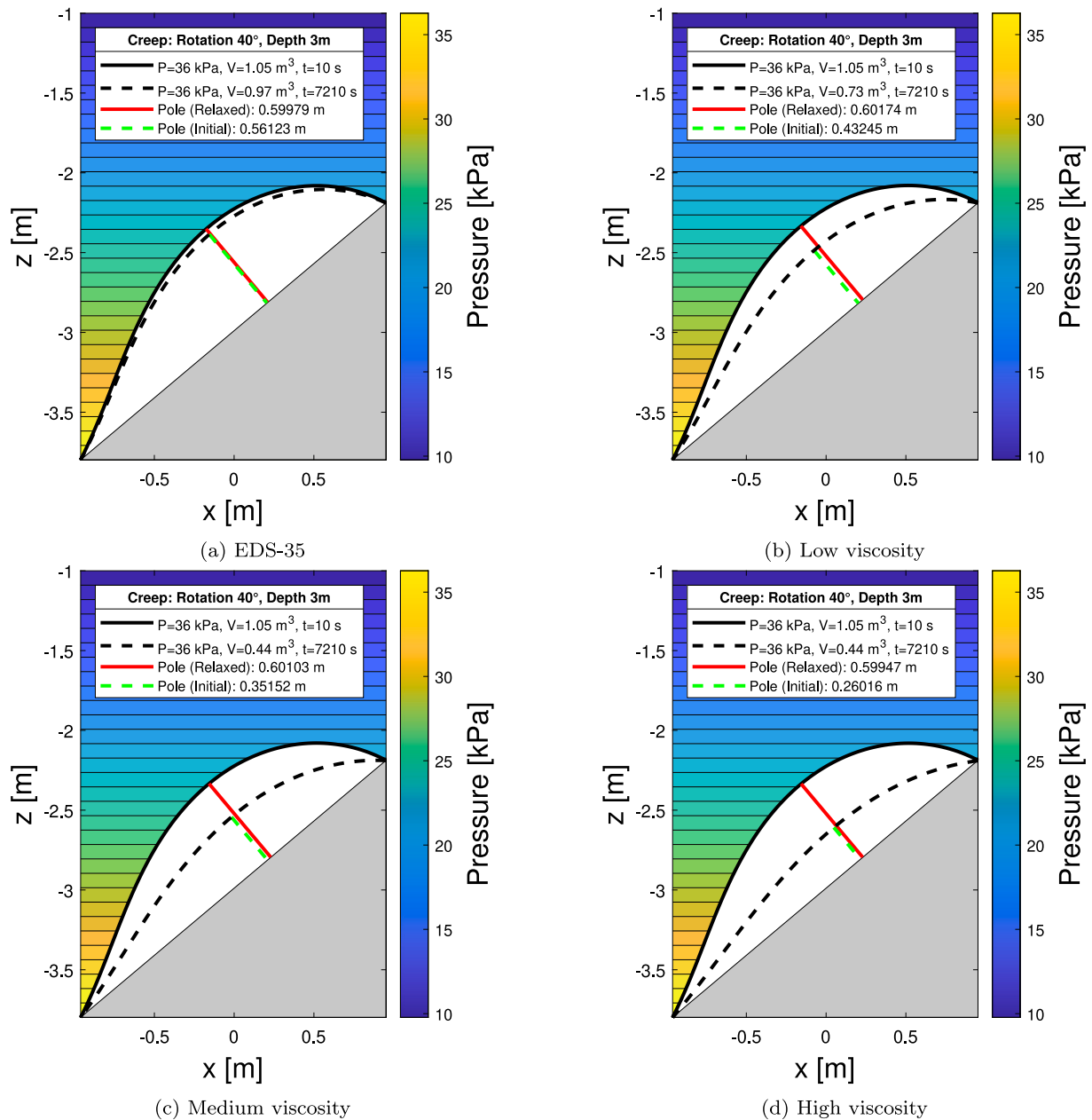


Fig. 17. Influence of material parameters on creep behaviour showing before and after positions at a depth of 3 m, pre-strain of 25% and orientation of 40°.

is applied to the bottom region of the membrane, the membrane pole position shifts relative to the rotation angle. As the pressure-differential is increased, the amount of creep increases after two hours. This is as a result of the higher stresses induced in the membrane. For an uneven shape, this concentrates around the pole of the membrane.

Another area to consider is the amount of pre-strain in the membrane; 25% and 50% are studied here at a depth of three metres as shown in Fig. 16. For a total internal pressures of 31–34 kPa (equivalent to a positive pressure-differential of 0.5–3.5 kPa), the amount of creep after two hours for the two pre-strains examined is significantly different. Firstly, the membrane deflection is larger at higher pre-strain values, and secondly, the membrane creep is greater. Since the strain and, thus, the stress are greater for 50%, this corresponds to an increase in the creep behaviour. It is also expected that the increased surface area for pressure to act on a thinner membrane material causes the greater membrane deflection.

6.2.2. Influence of viscoelastic parameters

As pointed out in the experimental and numerical contributions of this work, the EDS-35 compound exhibits very low amounts of viscoelasticity as desired for energy harvesting. To understand the effect of viscoelasticity on the creep membrane behaviour, an additional set of simulations are run using greater contributions for the viscous part (\bar{S}_v). Refer to Table 5 for details of the parameters analysed which starts with EDS-35, then ranges from a low to a high viscosity. All of these creep tests were done at an orientation of 40° relative to the water’s surface, a pre-strain of 25% and a internal pressure of 36 kPa; shown in Fig. 17. For this applied pressure, the baseline EDS-35 with little viscous behaviour exhibits negligible changes in the creep behaviour. There are notable increases in the creep behaviour as the viscosity increases. Since the elastic parameters are constant throughout all four studies, all final membrane shapes, i.e. after the material has completely relaxed, are identical as expected. The main difference is the initial starting point of the analyses, since the added viscosity increases the overall

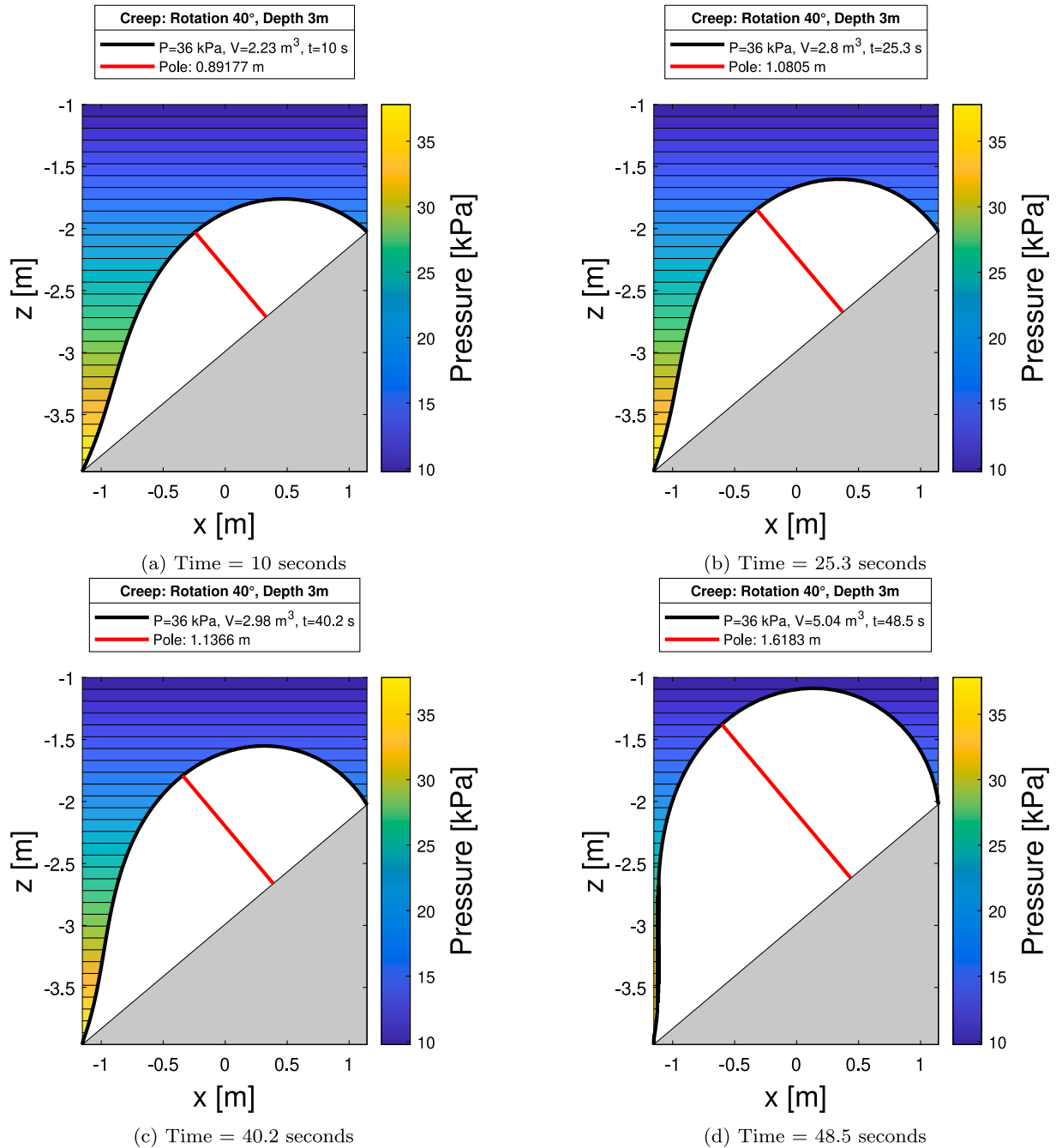


Fig. 18. Limit point instability of membrane as result of creeping with respect to time.

stiffness of the material initially. These tests beg the question of what initial inflation pressure is necessary to get to the desired relaxed response after several hours. Basing the operational characteristics solely on pole displacement may require significant pressure compensation with respect to time. This model includes the physical relaxation effect that is the creep over a short timespan, i.e. a few hours, until the equilibrium strain has been reached. The reality is that creep continues indefinitely throughout the operation, albeit at a lower rate than the initial physical relaxation effects (Mostafa et al., 2009; Oh and Kim, 2017). Long term creep as a result of degradation processes is not studied here, but it is something which should also be considered over longer time-scales of operation.

6.2.3. Influence on membrane instability

The change of P-V function highlights the risk of basing membrane displacement on hyperelastic parameters. For the EDS-35 material parameters, using a slightly higher pre-strain of 50% and inflating to a pressure of 36 kPa, the membrane passes the *limit point* stability as shown in Fig. 18. The membrane initially reaches a pole displacement of 0.89 m, over a period of 30 s, then it creeps to a pole displacement of 1.14 m, at which point the membrane begins to reach to the critical pressure for the material. In the next eight seconds, the pole displacement increases to 1.62 m, the volume of air within in the membrane doubles in 38 s, resulting in a catastrophic failure.

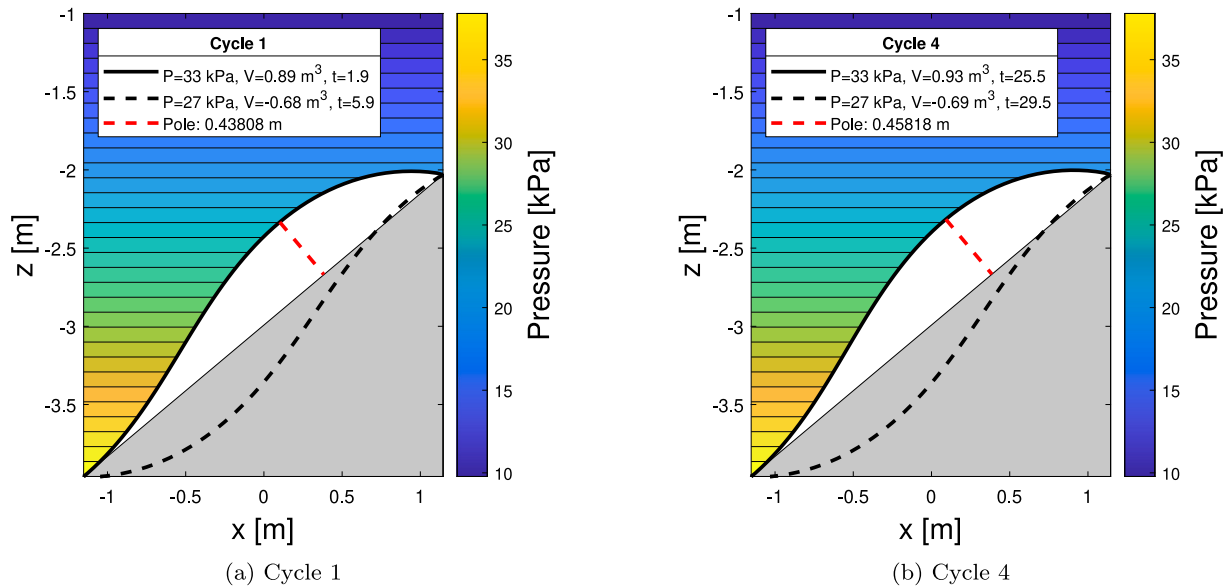


Fig. 19. Cyclic inflation for EDS-35 with a pre-strain of 50%.

Table 5

Viscous material parameters studied for membrane creep and dynamic simulations where m denotes the number of Maxwell elements. Note that the nonlinear relaxation parameter τ_v^{yh} was kept constant for all materials. Starting from left to right, the material parameters correspond to EDS-35, low viscosity, medium viscosity and high viscosity.

Viscous parameter	
c_v^{yh}	{0.03, 0.1, 0.2, 0.4} MPa
c_v^{nh}	{0.2(1m), 0.05(3m), 0.14(3m), 0.24(3m)} MPa
τ_v^{yh}	$\{\tau_{11} = 10, \tau_{12} = 3, k_{11} = 0.1, k_{12} = 72.04, k_{13} = 37.88,$ $k_{14} = 546.8, k_{15} = 276.3, k_{16} = 8.393, k_{17} = 2.297\}$ s (all)
τ_v^{nh}	{4(1m), 100(3m), 100(3m), 100(3m)} s

6.3. Cyclic test

The influence of the time-dependent material response is studied in an oscillating load case which mimics a real-world FlexWEC operational loading. This is an idealised case, whereby the inertial aspects of the dynamics are ignored, i.e. the added mass and damping matrix terms are not considered. Instead, just the influence of the time dependent stiffness matrix is studied under these quasi-static conditions.

6.3.1. Membrane deflection

During the inflation and deflation of the membrane, the material exhibits cyclic relaxation. Two simulations are run using different levels of viscous dissipation shown in Figs. 19 and 20, where the solid and dashed line represents the membrane shape for the inflation and deflation part of the cycle, respectively. For the EDS-35 parameters, the membrane is cycled with a sinusoidal pressurisation range of 27 to 33 kPa and a period of 7 s. It can be seen as softening of the material results in a minor change of deflection from 0.44 to 0.46 m, see Fig. 19. Increasing the viscosity to the 'high viscosity' studied in Section 6.2, results in more significant changes in the membrane deflection; 0.28 to 0.40 m, see Fig. 20. The membrane presents a different shape due to the increase in the internal pressure range from 22 to 38 kPa. Like the creep tests, the added stiffness from the viscosity component of the model is removed with time and loading regime. The membrane displacement and volume with respect to time is shown in Fig. 22(a). The amplitudes gradually get larger as time evolves for all materials.

6.3.2. Membrane hysteresis and phase-lag

As for the hysteretical behaviour, this is showcased in Fig. 21. Under this Neumann boundary condition, the hysteresis is relatively small but noticeable. This is true for both EDS-35 and the high viscosity parameters. As the material relaxes, this equates to smaller levels of hysteresis as time evolves. The phase-lag between the applied pressure and volume is compared for the high viscosity material at a 22 to 38 kPa pressure range, shown in Fig. 22(b). The phase-lag is minimal as a result of viscoelasticity. It is expected the inertial aspects from the fluid will dominate the phase-lag aspects of the operation which are not considered here.

7. Conclusion

In this article, three linked scientific stages are described. Firstly, a minimally dissipative unfilled natural rubber has been extensively experimentally characterised by various viscoelastic tensile test methods. The results of these experiments have been used to define a material (analytical) model and implemented in a finite element framework using nonlinear viscoelastic evolution laws. The final aspect of this work considered a submerged elastomeric membrane which represents the interesting new energy harvesting application of natural rubbers. The response to creep and cyclic tests with four materials, specifically, the identified material parameters as well as the response of three additional materials with higher levels of viscous dissipation have been predicted. Several conclusions can be drawn:

- A low dissipative polymer was chosen as part of the study since it offers a good baseline for further additional material analysis involving advanced filling solutions. It was found that unfilled natural rubber materials have limited rate-dependency but still show hysteresis and stress relaxation behaviour that cannot be discarded completely. It is expected the rate-dependency is greater at higher strain rates than the ones conducted in this study.
- The viscoelastic framework provided here is scalable, being able to not only capture polymers with a minimal viscous response but all also polymers with a high viscous response. This modelling framework can therefore be used to benchmark a wide range of future potential materials for FlexWEC applications.
- In the case studies presented here, even a low dissipative polymer has considerable nonlinear effects of interest to the application

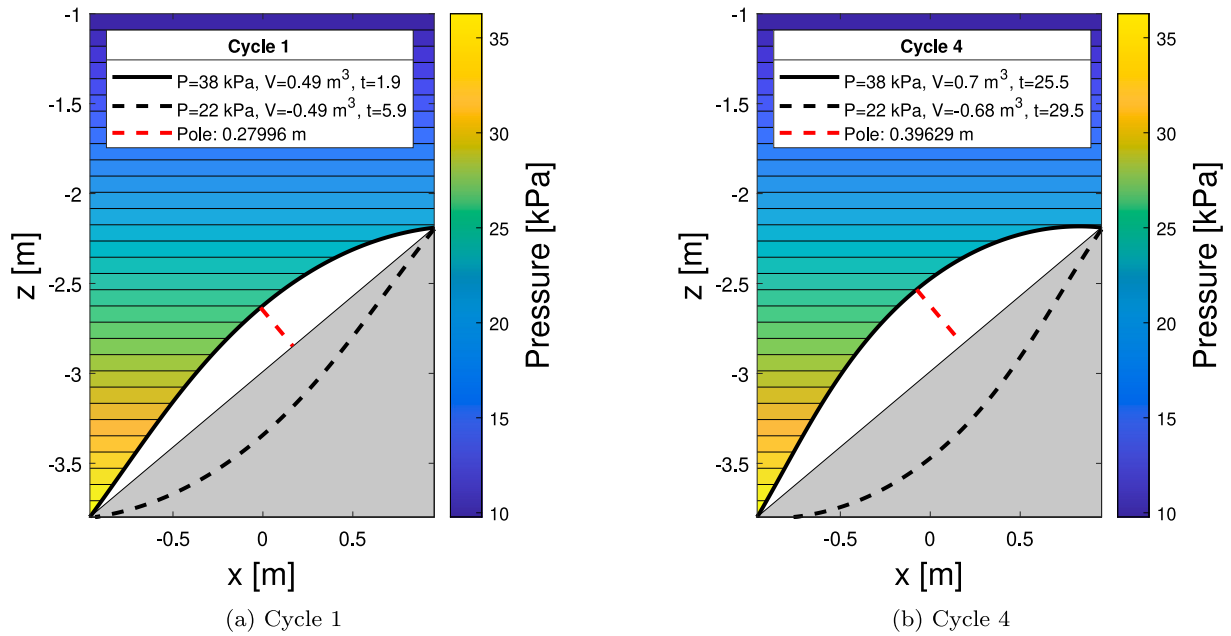


Fig. 20. Cyclic inflation for high viscosity with a pre-strain of 25%.

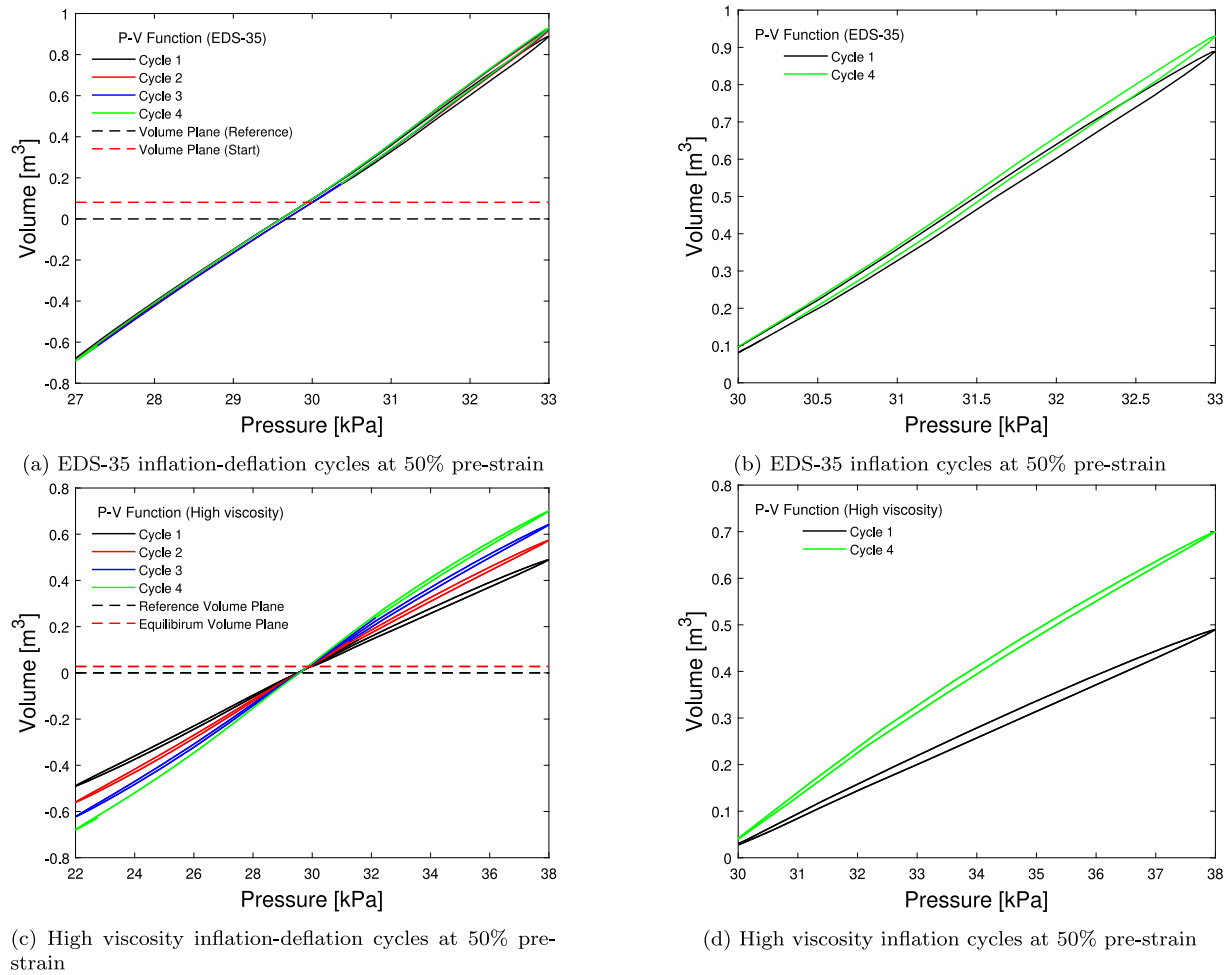
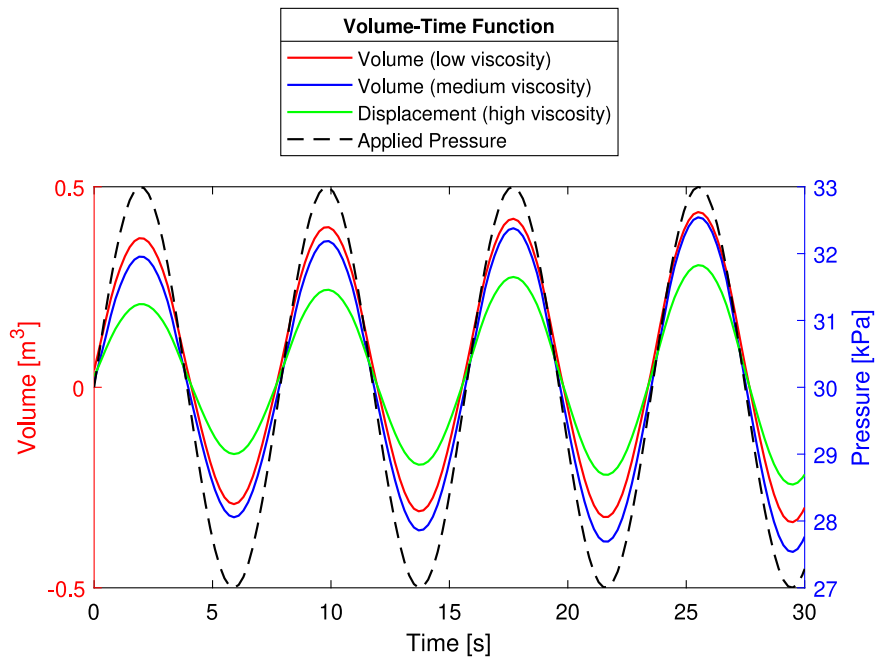
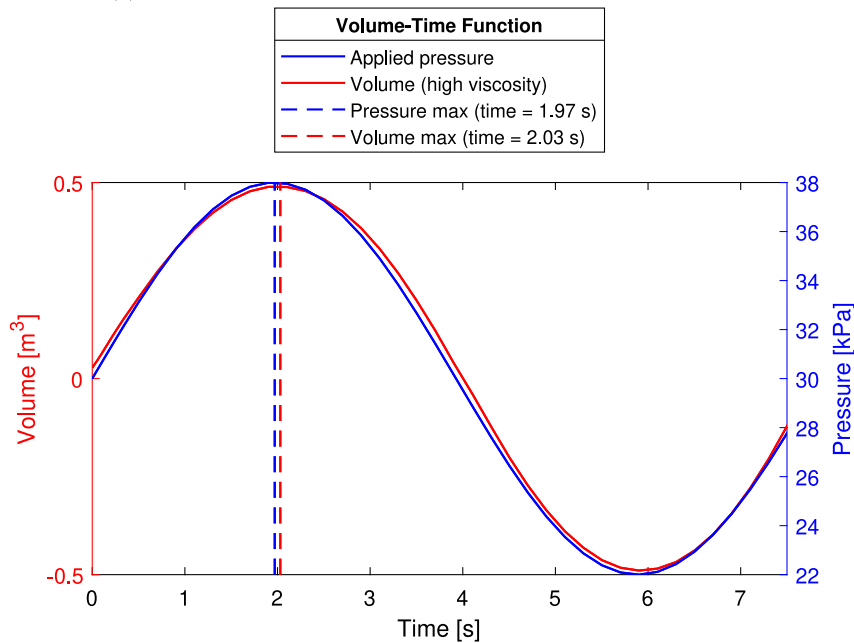


Fig. 21. Volume with respect to pressure up to 4 cycles for EDS-35 and high viscosity simulations.



(a) Low to high viscosity for an applied pressure range of 27-33 kPa



(b) High viscosity for an applied pressure range of 22-38 kPa

Fig. 22. Volume with respect to time for all materials studied.

studied. Creep behaviour can result in membrane instabilities occurring due to the changing stiffness with respect to the unloaded membrane material. In dynamic settings, time-dependent dissipative effects are observed proving that it cannot be ignored for calculating power capture.

Further works should calibrate the material at a wider range of strain rates under biaxial conditions to have more accurate predictions for this rate-dependency and dissipation behaviour. Importantly, the model can now be used to understand more clearly the stress response within flexible energy harvesting systems. This will support efforts for the development of sustainable sources of energy in the future.

Declaration of competing interest

The authors declare that they have no known competing financial interests or personal relationships that could have appeared to influence the work reported in this paper.

Data availability

Data will be made available on request.

Acknowledgements

The authors would like to thank Dr. Ing. Ralf Landgraf from Chemnitz University of Technology, Germany for his supports and inputs on

implementing the nonlinear evolution equation in the finite element framework. This research is supported by the Knowledge Economy Skills Scholarships (KESS 2). Knowledge Economy Skills Scholarships (KESS 2) is a pan-Wales higher level skills initiative led by Bangor University on behalf of the Higher Education sector in Wales. It is part funded by the Welsh Government's European Social Fund (ESF) convergence programme for West Wales and the Valleys. This study is also supported by EPSRC, United Kingdom through the Supergen ORE Hub (EP/S000747/1), who have awarded funding for the Flexible Fund project Submerged bi-axial fatigue analysis for flexible membrane Wave Energy Converters (FF2021-1036).

References

- Abaqus, 2014. 6.14 Documentation, Vol. 651. Dassault Systemes Simulia Corporation, (6.2).
- Algie, C., Ryan, S., Fleming, A., 2017. Predicted power performance of a submerged membrane pressure-differential wave energy converter. *Int. J. Mar. Energy* 20, 125–134.
- Amin, A., Lion, A., Sekita, S., Okui, Y., 2006. Nonlinear dependence of viscosity in modeling the rate-dependent response of natural and high damping rubbers in compression and shear: Experimental identification and numerical verification. *Int. J. Plast.* 22 (9), 1610–1657. <http://dx.doi.org/10.1016/j.ijplas.2005.09.005>.
- Anand, L., 1996. A constitutive model for compressible elastomeric solids. *Comput. Mech.* 18 (5), 339–355.
- Bechir, H., Chevalier, L., Chaouche, M., Boufala, K., 2006. Hyperelastic constitutive model for rubber-like materials based on the first Seth strain measures invariant. *Eur. J. Mech. A Solids* 25 (1), 110–124.
- Behnke, R., Kaliske, M., Klüppel, M., 2016. Thermo-mechanical analysis of cyclically loaded particle-reinforced elastomer components: experiment and finite element simulation. *Rubber Chem. Technol.* 89 (1), 154–176.
- Bergström, J.S., Boyce, M.C., 1998. Constitutive modeling of the large strain time-dependent behavior of elastomers. *J. Mech. Phys. Solids* 46 (5), 931–954.
- Bonet, J., Wood, R.D., 1997. *Nonlinear Continuum Mechanics for Finite Element Analysis*. Cambridge University Press.
- Bucchi, A., Hearn, G.E., 2013. Delay or removal of aneurysm formation in the Anaconda wave energy extraction device. *Renew. Energy* 55, 104–119.
- Carleo, F., Barbieri, E., Whear, R., Busfield, J.J., 2018. Limitations of viscoelastic constitutive models for carbon-black reinforced rubber in medium dynamic strains and medium strain rates. *Polymers* 10 (9), 988.
- Carleo, F., Plagge, J., Whear, R., Busfield, J., Klüppel, M., 2020. Modeling the full time-dependent phenomenology of filled rubber for use in anti-vibration design. *Polymers* 12 (4), 841.
- Carroll, M.M., 2010. A strain energy function for vulcanized rubbers. *J. Elasticity* 103 (2), 173–187. <http://dx.doi.org/10.1007/s10659-010-9279-0>.
- Chaplin, J., Heller, V., Farley, F., Hearn, G., Rainey, R., 2012. Laboratory testing the Anaconda. *Phil. Trans. R. Soc. A* 370 (1959), 403–424.
- Collins, I., Hossain, M., Dettmer, W., Masters, I., 2021. Flexible membrane structures for wave energy harvesting: A review of the developments, materials and computational modelling approaches. *Renew. Sustain. Energy Rev.* 151, 111478.
- Collins, I., Hossain, M., Masters, I., 2019. A review of flexible membrane structures for wave energy converters. In: *Proceedings of the 13th European Wave and Tidal Energy Conference (EWTEC 2019)*, Naples, Italy, pp. 1–6.
- Dal, H., Açıkan, A.K., Durcan, C., Hossain, M., 2022. An in silico-based review on anisotropic hyperelastic constitutive models for soft biological tissues. *arXiv preprint arXiv:2207.13985*.
- Dal, H., Acikgöz, Badienia, Y., 2021. On the performance of isotropic hyperelastic constitutive models for rubber-like materials: A state of the art review. *Appl. Mech. Rev.* 73 (2), 020802.
- Dippel, B., Johlitz, M., Lion, A., 2015. Thermo-mechanical couplings in elastomers—experiments and modelling. *ZAMM-J. Appl. Math. Mech./Z. Angew. Math. Mech.* 95 (11), 1117–1128.
- Dong, B., Liu, C., Wu, Y.-P., 2014. Fracture and fatigue of silica/carbon black/natural rubber composites. *Polym. Test.* 38, 40–45.
- Fehervary, H., Maes, L., Vastmans, J., Kloosterman, G., Famaey, N., 2020. How to implement user-defined fiber-reinforced hyperelastic materials in finite element software. *J. Mech. Behav. Biomed. Mater.* 110, 103737.
- Fu, X., Bu, T., Li, C., Liu, G., Zhang, C., 2020. Overview of micro/nano-wind energy harvesters and sensors. *Nanoscale* 12 (47), 23929–23944.
- Heng, F., Zhou, J., Gao, S., Jiang, L., 2021. Finite element simulation of the viscoelastic behavior of elastomers under finite deformation with consideration of nonlinear material viscosity. *Acta Mech.* 232, 4111–4132.
- Hoerner, S., Abbaszadeh, S., Cleynen, O., Bonamy, C., Maître, T., Thévenin, D., 2021a. Passive flow control mechanisms with bioinspired flexible blades in cross-flow tidal turbines. *Exp. Fluids* 62 (5), 1–14.
- Hoerner, S., Kösters, I., Vignal, L., Cleynen, O., Abbaszadeh, S., Maître, T., Thévenin, D., 2021b. Cross-flow tidal turbines with highly flexible blades—Experimental flow field investigations at strong fluid–structure interactions. *Energies* 14 (4), 797.
- Holzappel, G.A., 1996. On large strain viscoelasticity: continuum formulation and finite element applications to elastomeric structures. *Internat. J. Numer. Methods Engrg.* 39 (22), 3903–3926.
- Holzappel, G.A., 2000. *Nonlinear Solid Mechanics II*. John Wiley & Sons, Inc..
- Hossain, M., Amin, A., Kabir, M.N., 2015. Eight-chain and full-network models and their modified versions for rubber hyperelasticity: a comparative study. *J. Mech. Behav. Mater.* 24 (1–2), 11–24. <http://dx.doi.org/10.1515/jmbm-2015-0002>.
- Hossain, M., Liao, Z., 2020. An additively manufactured silicone polymer: Thermo-viscoelastic experimental study and computational modelling. *Addit. Manuf.* 35, 101395.
- Hossain, M., Navaratne, R., Perić, D., 2020. 3D printed elastomeric polyurethane: Viscoelastic experimental characterizations and constitutive modelling with nonlinear viscosity functions. *Int. J. Non-Linear Mech.* 126, 103546.
- Hossain, M., Steinmann, P., 2013. More hyperelastic models for rubber-like materials: consistent tangent operators and comparative study. *J. Mech. Behav. Mater.* 22 (1–2), <http://dx.doi.org/10.1515/jmbm-2012-0007>.
- Hossain, M., Vu, D.K., Steinmann, P., 2012. Experimental study and numerical modelling of VHB 4910 polymer. *Comput. Mater. Sci.* 59, 65–74.
- Huneau, B., 2011. Strain-induced crystallization of natural rubber: a review of X-ray diffraction investigations. *Rubber Chem. Technol.* 84 (3), 425–452.
- Johlitz, M., Scharding, D., Diebels, S., Retka, J., Lion, A., 2010. Modelling of thermo-viscoelastic material behaviour of polyurethane close to the glass transition temperature. *ZAMM-J. Appl. Math. Mech./Z. Angew. Math. Mech.: Appl. Math. Mech.* 90 (5), 387–398.
- Johlitz, M., Steeb, H., Diebels, S., Chatzouridou, A., Batal, J., Possart, W., 2007. Experimental and theoretical investigation of nonlinear viscoelastic polyurethane systems. *J. Mater. Sci.* 42 (23), 9894–9904.
- Kaliske, M., Rothert, H., 1997. Formulation and implementation of three-dimensional viscoelasticity at small and finite strains. *Comput. Mech.* 19 (3), 228–239.
- Kanner, L.M., Horgan, C.O., 2007. Elastic instabilities for strain-stiffening rubber-like spherical and cylindrical thin shells under inflation. *Int. J. Non-Linear Mech.* 42 (2), 204–215.
- Kleuter, B., Menzel, A., Steinmann, P., 2007. Generalized parameter identification for finite viscoelasticity. *Comput. Methods Appl. Mech. Engrg.* 196 (35–36), 3315–3334.
- Koprowski-Theiß, N., 2011. *Kompressible, viskoelastische werkstoffe: Experimente, modellierung und FE-umsetzung*.
- Koprowski-Theiß, N., Johlitz, M., Diebels, S., 2011. Modelling of a cellular rubber with nonlinear viscosity functions. *Exp. Mech.* 51 (5), 749–765.
- Kroon, M., 2010. A constitutive model for strain-crystallising rubber-like materials. *Mech. Mater.* 42 (9), 873–885.
- Kurniawan, A., Chaplin, J., Greaves, D., Hann, M., 2017. Wave energy absorption by a floating air bag. *J. Fluid Mech.* 812, 294–320.
- Landgraf, R., Shutov, A.V., Ihlemann, J., 2015. Efficient time integration in multiplicative inelasticity. *PAMM* 15 (1), 325–326.
- Le Cam, J.-B., 2017. Energy storage due to strain-induced crystallization in natural rubber: The physical origin of the mechanical hysteresis. *Polymer* 127, 166–173.
- Le Saux, V., Marco, Y., Bles, G., Calloch, S., Moyné, S., Plessis, S., Charrier, P., 2011. Identification of constitutive model for rubber elasticity from micro-indentation tests on natural rubber and validation by macroscopic tests. *Mech. Mater.* 43 (12), 775–786.
- Liao, Z., Hossain, M., Yao, X., Mehnert, M., Steinmann, P., 2020. On thermo-viscoelastic experimental characterization and numerical modelling of VHB polymer. *Int. J. Non-Linear Mech.* 118, 103263.
- Linder, C., Tkachuk, M., Miehe, C., 2011. A micromechanically motivated diffusion-based transient network model and its incorporation into finite rubber viscoelasticity. *J. Mech. Phys. Solids* 59 (10), 2134–2156. <http://dx.doi.org/10.1016/j.jmps.2011.05.005>.
- Lion, A., 1997. A physically based method to represent the thermo-mechanical behaviour of elastomers. *Acta Mech.* 123 (1), 1–25.
- Liu, H., Holzappel, G.A., Skallerud, B.H., Prot, V., 2019. Anisotropic finite strain viscoelasticity: Constitutive modeling and finite element implementation. *J. Mech. Phys. Solids* 124, 172–188.
- Lubliner, J., 1985. A model of rubber viscoelasticity. *Mech. Res. Commun.* 12 (2), 93–99.
- Marckmann, G., Verron, E., 2006. Comparison of hyperelastic models for rubber-like materials. *Rubber Chem. Technol.* 79 (5), 835–858.
- Miehe, C., 1996. Numerical computation of algorithmic (consistent) tangent moduli in large-strain computational inelasticity. *Comput. Methods Appl. Mech. Engrg.* 134 (3–4), 223–240.
- Miehe, C., Keck, J., 2000. Superimposed finite elastic–viscoelastic–plastoelastic stress response with damage in filled rubbery polymers. Experiments, modelling and algorithmic implementation. *J. Mech. Phys. Solids* 48 (2), 323–365.
- Moretti, G., Fontana, M., Verthey, R., 2015. Model-based design and optimization of a dielectric elastomer power take-off for oscillating wave surge energy converters. *Meccanica* 50 (11), 2797–2813.
- Moretti, G., Herran, M.S., Forehand, D., Alves, M., Jeffrey, H., Verthey, R., Fontana, M., 2020. Advances in the development of dielectric elastomer generators for wave energy conversion. *Renew. Sustain. Energy Rev.* 117, 109430.

- Mostafa, A., Abouel-Kasem, A., Bayoumi, M., El-Sebaie, M., 2009. On the influence of CB loading on the creep and relaxation behavior of SBR and NBR rubber vulcanizates. *Mater. Des.* 30 (7), 2721–2725.
- Mullins, L., 1948. Effect of stretching on the properties of rubber. *Rubber Chem. Technol.* 21 (2), 281–300.
- Niemczura, J., Ravi-Chandar, K., 2011a. On the response of rubbers at high strain rates—I. Simple waves. *J. Mech. Phys. Solids* 59 (2), 423–441.
- Niemczura, J., Ravi-Chandar, K., 2011b. On the response of rubbers at high strain rates—II. Shock waves. *J. Mech. Phys. Solids* 59 (2), 442–456.
- Niemczura, J., Ravi-Chandar, K., 2011c. On the response of rubbers at high strain rates—III. Effect of hysteresis. *J. Mech. Phys. Solids* 59 (2), 457–472.
- Oh, J., Kim, J.H., 2017. Prediction of long-term creep deflection of seismic isolation bearings. *J. Vibroeng.* 19 (1), 355–362.
- Patil, A., 2016. Inflation and Instabilities of Hyperelastic Membranes (Ph.D. thesis). KTH Royal Institute of Technology.
- Reese, S., Govindjee, S., 1997. Theoretical and numerical aspects in the thermo-viscoelastic material behaviour of rubber-like polymers. *Mech. Time-Depend. Mater.* 1 (4), 357–396.
- Reese, S., Govindjee, S., 1998. A theory of finite viscoelasticity and numerical aspects. *Int. J. Solids Struct.* 35 (26–27), 3455–3482. [http://dx.doi.org/10.1016/s0020-7683\(97\)00217-5](http://dx.doi.org/10.1016/s0020-7683(97)00217-5).
- Rosati Papini, G.P., Moretti, G., Vertechy, R., Fontana, M., 2018. Control of an oscillating water column wave energy converter based on dielectric elastomer generator. *Nonlinear Dynam.* 92 (2), 181–202.
- Scheffer, T., Goldschmidt, F., Diebels, S., 2015a. Implementation of the strongly pronounced non-linear viscoelasticity of an incompressible filled rubber. *Tech. Mech.* (ISSN: 2199-9244) 35 (2), 118–132. <http://dx.doi.org/10.24352/UB.OVGU-2017-074>, 35; 2; 119-132.
- Scheffer, T., Goldschmidt, F., Diebels, S., 2015b. Characterisation of filled rubber with a pronounced non-linear viscoelasticity. *PAMM* 15 (1), 353–354. <http://dx.doi.org/10.1002/pamm.201510167>.
- Shutov, A.V., Landgraf, R., Ihlemann, J., 2013. An explicit solution for implicit time stepping in multiplicative finite strain viscoelasticity. *Comput. Methods Appl. Mech. Engrg.* 265, 213–225.
- Simo, J.C., 1987. On a fully three-dimensional finite-strain viscoelastic damage model: formulation and computational aspects. *Comput. Methods Appl. Mech. Engrg.* 60 (2), 153–173.
- Steinmann, P., Hossain, M., Possart, G., 2012. Hyperelastic models for rubber-like materials: consistent tangent operators and suitability for Treloar's data. *Arch. Appl. Mech.* 82 (9), 1183–1217. <http://dx.doi.org/10.1007/s00419-012-0610-z>.
- Wang, S., Chester, S.A., 2018. Experimental characterization and continuum modeling of inelasticity in filled rubber-like materials. *Int. J. Solids Struct.* 136, 125–136.
- Wei, L., Fu, X., Luo, M., Xie, Z., Huang, C., Zhou, J., Zhu, Y., Huang, G., Wu, J., 2018. Synergistic effect of CB and GO/CNT hybrid fillers on the mechanical properties and fatigue behavior of NR composites. *RSC Adv.* 8 (19), 10573–10581.
- Yeoh, O.H., 1993. Some forms of the strain energy function for rubber. *Rubber Chem. Technol.* 66 (5), 754–771.
- Zhang, S., Zheng, L., Liu, D., Xu, Z., Zhang, L., Liu, L., Wen, S., 2017. Improved mechanical and fatigue properties of graphene oxide/silica/SBR composites. *RSC Adv.* 7 (65), 40813–40818.
- Zhou, J., Jiang, L., Khayat, R.E., 2018. A micro–macro constitutive model for finite-deformation viscoelasticity of elastomers with nonlinear viscosity. *J. Mech. Phys. Solids* 110, 137–154.